Studying the 2H to 1T′ phase transition of monolayer MoS_2 on gold using Low Energy Electron Microscopy

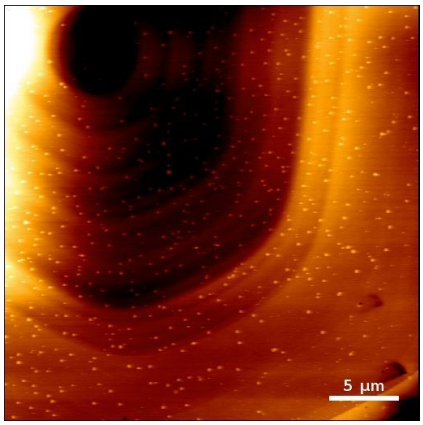

THESIS

submitted in partial fulfillment of the
requirements for the degree of

BACHELOR OF SCIENCE
in
PHYSICS

Author :	Renee van Limpt
Student ID :	1774557
Supervisor :	Vera Janssen, Msc
	Dr. Johannes Jobst
2^{nd} corrector :	Prof. dr. Jan M. van Ruitenbeek

Leiden, The Netherlands, June 18, 2019

Studying the 2H to 1T′ phase transition of monolayer MoS_2 on gold using Low Energy Electron Microscopy

Renee van Limpt

Huygens-Kamerlingh Onnes Laboratory, Leiden University
P.O. Box 9500, 2300 RA Leiden, The Netherlands

June 18, 2019

Abstract

The coexistence of the semi-conducting 2H and quasi-metallic 1T′ monolayer MoS_2 phases has great potential in, for example, low-resistance contacts. In this research MoS_2 on gold samples have been fabricated. Several different fabrication procedures have been tested including stamping, gold-mediated exfoliation and hydrogen plasma cleaning. Measurements identifying the 2H phase have been made using Atomic Force Microscopy and Low Energy Electron Microscopy. Although 1T′ could not be observed, insights are gained into the various fabrication processes.

Contents

Chapter 1

Introduction

In 2004, the Nobel Prize was awarded to Andre Geim and Konstantin Novselov for their groundbreaking experiments on the two-dimensional variant of graphite: graphene [1]. The discovery of graphene led to an explosive growth in the research on two-dimensional materials.

Two-dimensional materials can be isolated from so called van der Waals materials which are layered crystalline materials. A van der Waals material consists of multiple two-dimensional layers held together by the relatively weak van der Waals interaction instead of the common ionic or covalent bonds. The atoms within the unit layer are bound by the strong covalent bonds. These distinctive properties allow for exfoliation of single layers of material: the so-called 2D materials. The extreme case of surface science determines the physics of these materials as there is no bulk material between the surface layers [2]. The reduction to two dimension allows for exceptional electronic, optical and magnetic properties which offers opportunities for applications such as low-power devices. The world of two-dimensional materials is very divers as illustrated by the fact that it contains metals, semi-conductors and insulators (figure 1.1). The combination of monolayers of different materials (called heterostructures) offers even more possibilities and allows for exploration of novel quantum effects [3].

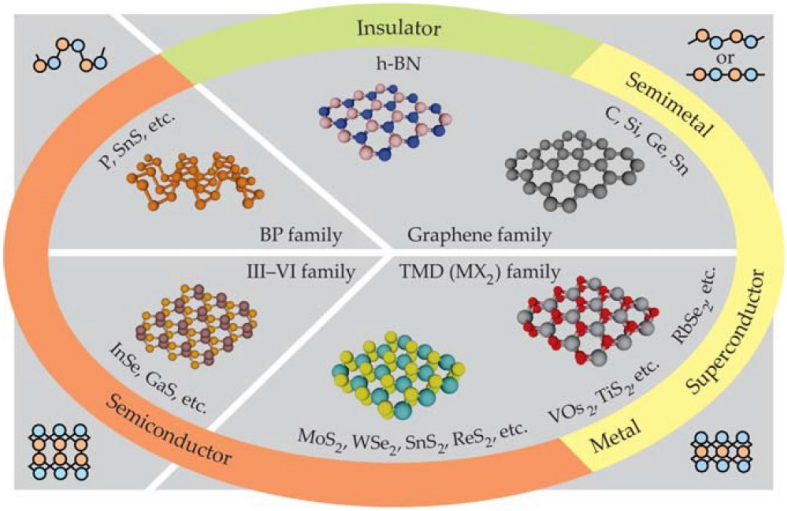

Figure 1.1: *The different types of two-dimensional materials with their respective electronic properties and a generic overview of the unit cell structures. Taken from [3]*

One of these two-dimensional materials is molybdenum disulphide (MoS_2). MoS_2 belongs to the class of transition metal dichalcogenides (TMDs). TMD unit layers consist of three covalently bonded atomic layers; the transition metal (M) is set between two chalcogen (X) layers (figure 1.2) giving it the MX_2 form. For MoS_2 the transition metal is molybdenum and the chalcogen is sulphur[4]. Although these exfoliated single unit layers consist of multiple atomic layers, they are called two-dimensional materials and their physics is different from their three dimensional counterparts. An interesting property of these two-dimensional TMDs is that different structural phases can occur. There are, for example, a trigonal prismatic (hexagonal, H), octahedral (tetragonal, T) and a distorted phase (T'), as illustrated in figure 1.3 [5].

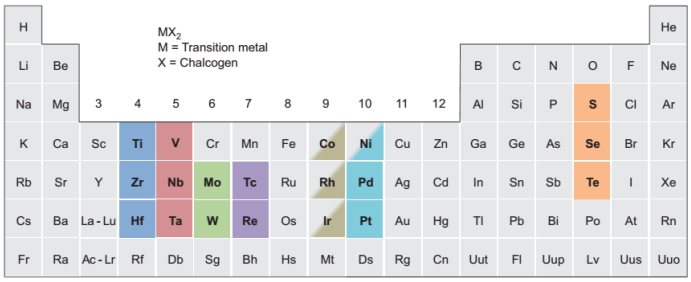

Figure 1.2: *Periodic table of elements. Highlighted are the most common transition metals and the three chalcogens. Co, Rh, Ir and Ni are partially highlighted as they only form van der Waals materials with some chalcogens.*
Adapted from [6].

The different phases result in different material properties. The 2H phase (where the digit represents the number of monolayers in the unit cell [7]) is a semiconductor whilst both the 1T and 1T′ phase are (quasi)metallic [8]. Furthermore, the 2H and 1T′ states are both stable whilst the 1T phase is not: it will decay into the 1T′ state. Transformation from to 2H to the 1T′ phase can be caused by doping, strain or temperature [9].

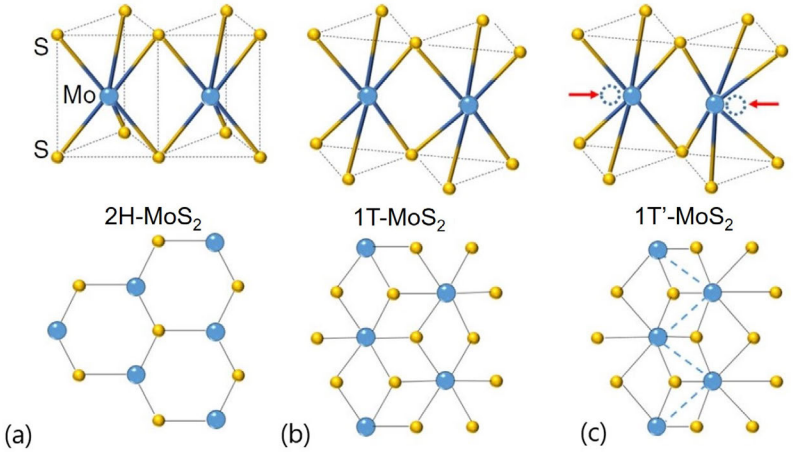

Figure 1.3: *The (a) 1H, (b) 1T and (c) 1T′ phases of MoS_2. The blue dotted line indicates the transformation from 1T to 1T′ MoS_2.*
Adapted from [8]

During the last few years, 2H MoS_2 has shown potential to be used in various applications such as transistors [10], photodetectors [11] and solar cells [4, 12]. An advantage of TMDs (and therefore of MoS_2) is the possibility for 2H and 1T(′) to coexist within a layer. This way, for example, low-resistance contacts between semiconductors and electrodes can be created. This can be done by locally transforming the 2H phase into 1T(′) MoS_2 which has much reduced contact resistance compared to most metals used for contacts due to its semimetallic nature. The direct contact between 2H and 1T(′) phase eliminates the high resistance (0.7 kΩµm - 10 kΩµm[13]) van der Waals gap tunnelling barrier present when using other metal contacts on 2H-MoS_2 [13, 14].
These contacts obviously rely on the characteristics of the 2H to 1T′ phase transition such as transformation yield and coexistence of phases. It is therefore paramount that besides understanding both structural phases also the transition between these phases is understood. Currently both the 2H and 1T′ phase are relatively well comprehended but the actual transition between both states is not.

In this research, samples are fabricated that consists of a single crystalline bulk gold plate with a monolayer MoS_2 on top. The samples are heated to study the 2H to 1T' phase transition. Therefore a technique must be found that can image at the interface between gold and MoS_2. An quintessential tool to study surfaces and a few layers of materials is Low Energy Electron Microscopy (LEEM). Furthermore it is also possible to heat the samples in situ which allows for live measurements of the phase transition.
Therefore, the samples are optimized for LEEM investigations. Furthermore, Atomic Force Microscopy (AFM) has been used to extensively characterize the sample morphology. Finally, the phase transition is characterized using LEEM.

Chapter 2

Theory

2.1 Molybdenum disulphide

The TMD MoS_2 consists of multiple monolayers bonded by the weak van der Waals force. Within a monolayer there are different possible orientations for the molybdenum in regard to the sulphur. The three known polytypes are hexagonal (H), rhombohedral (R) and trigonal (face centred cubic, T). Each polytype is combined with a number that reflects the amount of layers in a single crystallographic unit cell. This results in a 2H, 3R and 1T structural phase for MoS_2 as visualised in figure 2.1 [15]. In hexagonal monolayers the inversion symmetry between the layers is lost which turns the 2H phase to 1H phase. In literature, however, monolayer 1H MoS_2 is often referred to as 2H in order to connect it to the bulk state. This convention is also followed in this thesis. The phase transition studied in this research is from the 2H to the 1T′ phase.

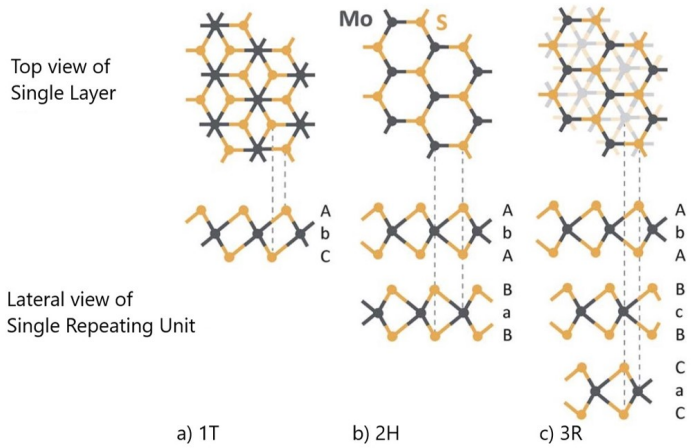

Figure 2.1: *Top and lateral view of the (bulk) MoS_2 polytypes. The dashed lines demonstrates the match between the lateral and top view. In 3R MoS_2 (c) the atoms that do not overlap are represented in grey scales in the top view.*
Taken from [15]

The 2H phase is the naturally available phase and is a indirect semiconductor with a 1.2 eV bandgap when encountered in bulk. In a monolayer however, 2H MoS_2 becomes a direct semiconductor with a bandgap of 1.7 eV as depicted in figure 2.2 [7]. This semiconducting nature has given rise to many possible applications. Due to the high current on/off ratio (1×10^8 at room temperature) and mobilities up to 200 $cm^2/(Vs)$, MoS_2 has great potential in, for example, transistors, optoelectronics, transparent and bendable electronics and energy harvesting [10].

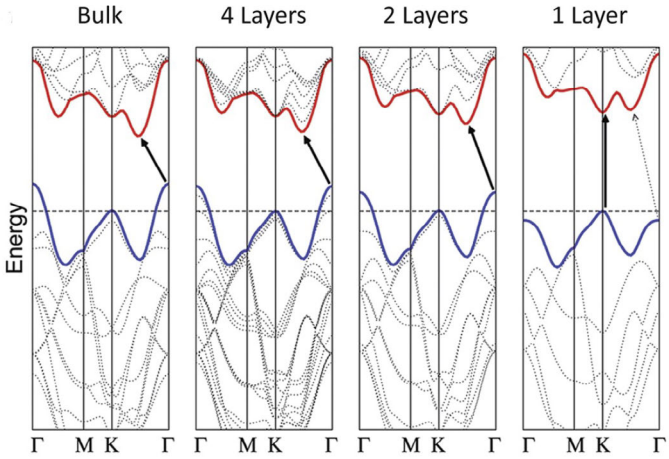

Figure 2.2: *Calculated electronic band structure for different thicknesses of 2H MoS_2. The arrows indicates the transition from an indirect to a direct bandgap. Taken from [15]*

Whereas 2H MoS_2 is stable, 1T MoS_2 is not and will often decay to the 1T' MoS_2 superstructure (figure 2.3). The instability of 1T can be predicted from the theoretically calculated formation energy per atom. For the 2H to 1T transformation this is 0.28 eV/atom whilst for the 2H to 1T' phase transition, a value of 0.18 eV/atom is found. This latter is therefore energetically favourable and accordingly the expected state. Whereas 1T is a metal, 1T' is a quasi-metallic material with a bandgap of 50 meV [7, 16].The properties of (stabilized) 1T MoS_2 are such that they have been used in field effect transistors [13], supercapacitors [17] and electrocatalysts [18].

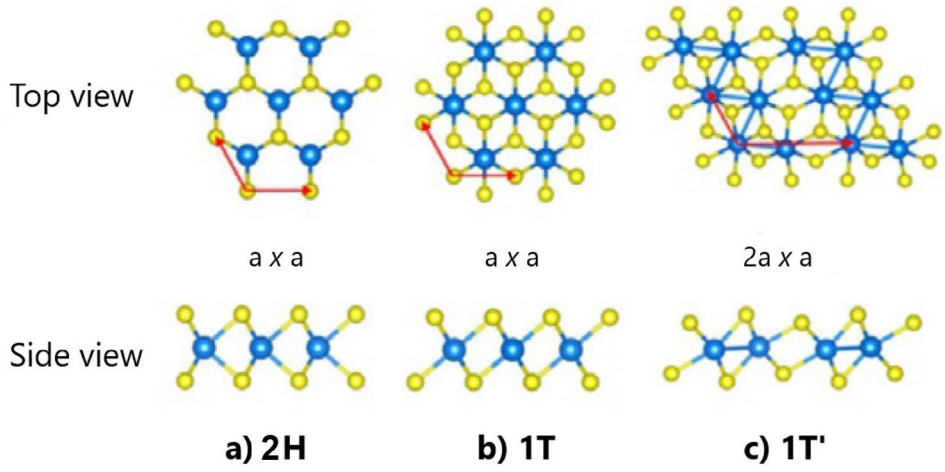

Figure 2.3: *Overview of some monolayer MoS_2 polymorphs: 2H (a), 1T (b) and 1T'(c). 1T' is the distorted phase of 1T MoS_2. The red arrows indicate the the unit cells, the blue spheres are molybdenum and the yellow ones sulphur.*
Taken from [7]

The phase transition from 2H to 1T(') is investigated using gold as it lowers the transition temperature using interfacial strain and the transfer of electrons to monolayer MoS_2 [8].
When MoS_2 contacts the gold, electrons start to transfer from the gold to the monolayer which causes a charge accumulation at the sulphur and charge depletion between the sulphur and molybdenum layers (figure 2.4(a)). The introduction of the gold also initiates interfacial strain. When MoS_2 experiences tensile strain it inhibits an increase in electron affinity [19]. The introduction of gold, therefore, activates this electron affinity effect making a increased charge transfer possible. A further indication of this cooperation between strain and charge transfer lies in the fact that 1T'-MoS_2 is favoured at smaller electron doping concentrations when it experiences tensile strain as compared to the unstrained case [8].

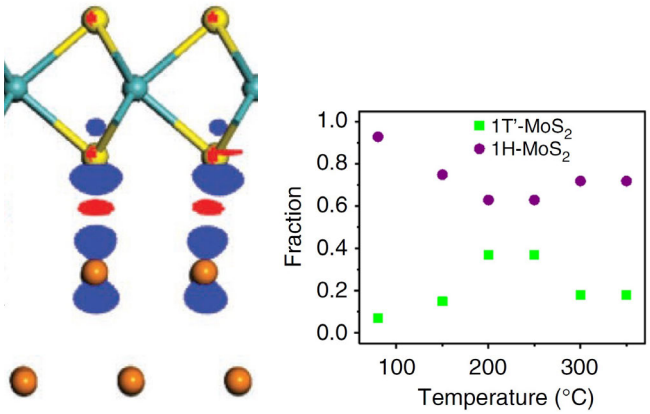

(a) *Adapted from [20].* ***(b)*** *Adapted from [8].*

Figure 2.4: *(a) visualises the dynamic (DFT) simulated charge distribution of MoS_2 on gold. Atoms are represented as spheres (Mo in teal, S in yellow, Au in orange), the charge accumulation regions as red areas and the charge depletion regions as blue areas. (b) demonstrates the temperature dependence of the 2H to 1T′ phase transition of monolayer MoS_2.*

The charge transfer indicates that the internal Mo-S bonds become weakened which in turn facilitates the 2H to 1T′ transition. There, however, is one major setback: the formation of an interfacial tunnel barrier between gold and MoS_2 makes it necessary to insert extra energy to induce this electron transfer. This extra energy is inserted through heating. As too much induced energy may lead to disassembly of the atomic structure, there is a optimal transition temperature. For gold, this point is experimentally determined to be at 250°C [8]. The phase transition causes the sulphur atoms at the edge to move to the centre whilst the central sulphur atoms move to the edge (see figure 2.5). This also causes the molybdenum atom to shift slightly causing the 1T′ phase to be formed [20]. For mixed phase $MoS_(2)$ on gold the percentage 1T′ phase present in monolayer MoS_2 increases from ≈7% during creation to ≈37% at the temperature optimum of 250°C (figure 2.4(b)) [8].

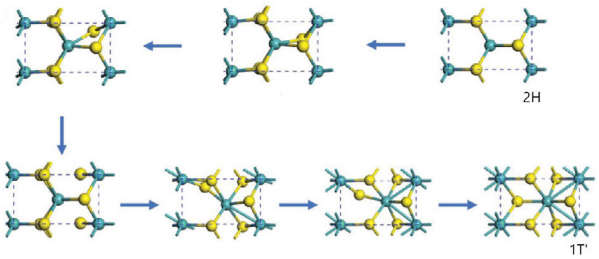

Figure 2.5: *Dynamic simulations of the 2H (first image) to 1T′ (last image) phase transition. Molybdenum is represented by teal spheres and sulphur by yellow ones. Adapted from [20].*

2.2 Electron diffraction

As both gold and MoS_2 have a crystal nature, a well defined lattice constant and diffraction pattern are expected to be measured. The measured diffraction patterns reflect the atomic arrangement from a topview. Therefore, differences between 2H, 1T and 1T' MoS_2 are expected to be seen (see figure 2.3). As visualised, the expected diffraction pattern for 2H-MoS_2 is hexagonal. Gold is known to have a face-centred cubic Bravais lattice which indicates that a hexagonal diffraction structure is also expected when the surface orientation of the gold is (111). To further investigate the nature of the materials, a lattice constant calculation can be made.

The kinetic energy of electrons in vacuum is specified by the dispersion relation:

$$E_k = \frac{\hbar^2 |\mathbf{k}|^2}{2m_e} \tag{2.1}$$

Where E_k is the electron kinetic energy, $\hbar$ the reduced Planck constant, m_e the electron mass and $\mathbf{k}$ is the wave vector which is related to the wavelength as $|\mathbf{k}| = \frac{2\pi}{\lambda}$. In order for the wave vector to interfere with the hexagonal lattice, it is necessary to fulfil the Laue condition which states that the difference in parallel wave vector ($\mathbf{k} = \mathbf{k}^{\perp} + \mathbf{k}^{\parallel}$) must be equal to the reciprocal lattice vector $\mathbf{G}_{lm}$:

$$\mathbf{k}^{\parallel}_{out} - \mathbf{k}^{\parallel}_{in} = \mathbf{G}_{lm} = l\mathbf{a}^*_1 + m\mathbf{a}^*_2 \tag{2.2}$$

Where $\mathbf{a}^*_1$ and $\mathbf{a}^*_2$ are the reciprocal lattice vectors which relate to their real space equivalents as

$$\mathbf{a}^*_1 = \frac{2\pi \mathbf{a}_2 \times \hat{\mathbf{n}}}{|\mathbf{a}_1 \times \mathbf{a}_2|} \qquad \mathbf{a}^*_2 = \frac{2\pi \mathbf{a}_1 \times \hat{\mathbf{n}}}{|\mathbf{a}_2 \times \mathbf{a}_1|} \tag{2.3}$$

When measuring in diffraction space using LEEM, the first order diffraction spots appear only at higher energies. This is because the electrons need to gain energy (as momentum) in order to be able to exit the lattice again. This indicates that the energy of the incoming electrons must equal to the reciprocal lattice vector when the diffraction spots first appear.

$$\mathbf{G}_{lm} \leq |\mathbf{k}| = \frac{\sqrt{2m_e E_k}}{\hbar} \tag{2.4}$$

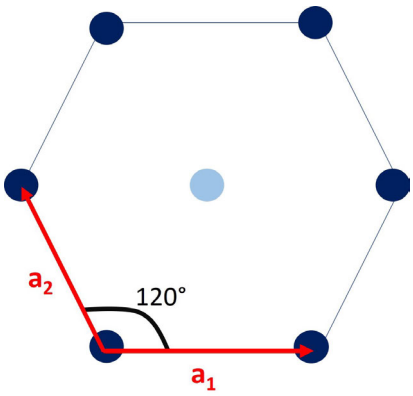

Figure 2.6: *An illustration of the lattice vectors in a hexagonal lattice*

Because of the hexagonal nature of the measured diffraction pattern, the lattice constant $a = |\mathbf{a}_1| = |\mathbf{a}_2|$ and the angle between $\mathbf{a}_1$ and $\mathbf{a}_2$ is 120° (see figure 2.6). When this information is inserted in equation 2.4 for either primary diffraction spot ((0,1) or (1,0)) the following relation between the lattice constant and reciprocal lattice vector is obtained:

$$|\mathbf{G}_{01}| = \mathbf{a}_2^* = \frac{2\pi a}{a^2 \sin 120^\circ} = \frac{4\pi}{\sqrt{3}a} \tag{2.5}$$

When combined with the dispersion relation and the realisation that $\hbar = \frac{h}{2\pi}$ the following lattice constant is found:

$$a = \frac{2h}{\sqrt{6m_e E_k}} \tag{2.6}$$

With electron mass $m_e \approx 9.109 \times 10^{-31}$kg, Planck constant $h = 6.626 \times 10^{-34}$m^{2}kg/s and E the energy at which the first order diffraction spots appear [21].

For MoS_2 this formula holds. For gold, however, one must realize that the hexagonal lattice is a result of the orientation and the actual structure is a face-centred cubic (FCC) crystal. To relate this inter-planar distance to the actual lattice constant the relation $d = \frac{a}{\sqrt{h^2+k^2+l^2}} = \frac{a}{\sqrt{3}}$ is used, where a is the lattice constant, h, k, l are the Miller indices and d is the inter-planar distance (previously calculated as a). The FCC orientation allows only for reflections when h, k, l are all odd or all even. When the first order diffraction spots are selected the adapted equation becomes

$$a = \frac{\sqrt{2}h}{\sqrt{m_e E_k}} \tag{2.7}$$

Chapter 3

Sample fabrication and experimental techniques

In order to research the 2H to 1T′ phase transition samples consisting of gold with a monolayer MoS_2 on top have been fabricated using various techniques. Two different gold plates and two exfoliation methods for MoS_2 have been used. The sample fabrication relies on the experimental stamping and gold-mediated exfoliation techniques. These are therefore discussed first. Subsequently the two gold plates and the exfoliation methods are reviewed. Finally, the fabricated samples are presented.

3.1 Experimental techniques

3.1.1 Stamping

Stamping is a technique to transport thin flakes. In this research the 2D heterostructure transfer system from HQ graphene is used.
To transport a flake a glass slide is prepared with a polydimethylsiloxane (PDMS) block coated with polycarbonate (PC) to create an adhesive layer [22, 23]. When brought in contact and heated to 120°C, the PC coats an adhesive layer over to sample enabling it to be lifted (figure 3.1).
After lifting, the flake also needs to be dropped again. This is done by placing it on the desired substrate and heating the sample to 180°C. This allows for the PC to melt whilst the PDMS stays intact. The coated sample is finally cleaned using chloroform to remove the PC. For detailed information about the preparation process see appendix A.2.

The stamping process is designed for two-dimensional materials and therefore ideal for (monolayer) MoS_2. In order to move thicker gold microplates (thicknesses between 30 and 1000 nm [24]) an adaptation has been made. When using the standard square PDMS cut-out, the placement of the contact point is not very precise and when the contact point falls besides the microplate, an air

bubble will be formed and the platelet cannot be picked up (as the PC does not touch the gold, see figure 3.2). It is therefore necessary to create a sharper tip to decrease the placement error. Therefore, a triangular shape is cut out of the PDMS (see appendix A.2).

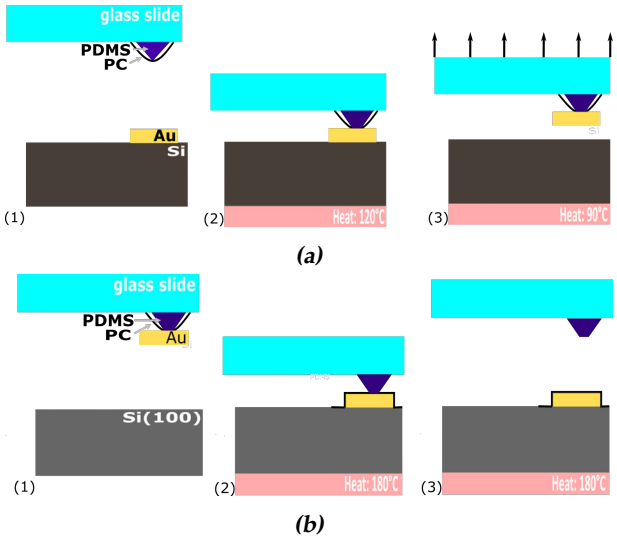

Figure 3.1: *A schematic representation (not to scale) of the transportation process for gold microplates.*
(a) The lift-off process. (1) The PC is lowered onto the gold until interference patterns which indicate that the materials almost touch are visible. (2) Then the gold plate is heated till 120°C to secure the bonding between the gold and PC. (3) Finally the temperature is decreased to 90°C and the gold is lifted of the silicon substrate.
(b) The drop-down process. (1) The gold is lowered onto the Si(100) wafer. (2) Next the substrate is heated till 180°C to melt the PC (but not the PDMS). (3) Finally the PDMS is lifted up and the PC coated gold is left on the wafer.

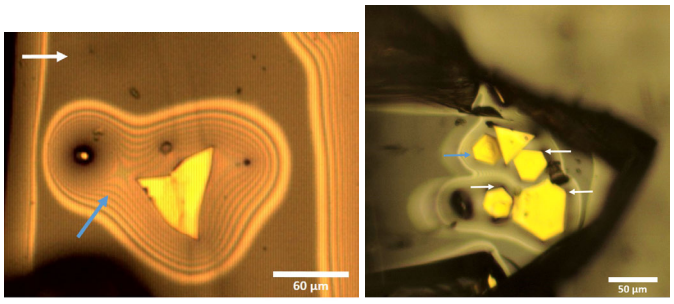

Figure 3.2: *(a) shows the air bubble formed around the gold particle when the gold is not the first contact point, (b) indicates the contact between the PC and gold. Blue arrows shows the interference patterns that indicate no contact and white arrows indicate contact between PC and the substrate.*

3.1.2 Gold-mediated exfoliation

Gold is known to have a strong affinity for chalcogens (oxygen, sulphur, selenium, tellurium and polonium). This affinity is especially strong for sulphur atoms; it forms a semi-covalent bond [25]. In MoS_2 the sulphur atoms are situated at the surface of the crystal (see figure 2.1). This allows for bonding when it is brought in contact with gold. The semi-convalent bond is stronger than the weak van der Waals bonds between the internal MoS_2 unit layers which leads to exfoliation of monolayers of MoS_2 when both materials are separated again.

When however, the gold surface is contaminated, the bond between the Au and MoS_2 weakens. First, the bonds become comparable to those between the intermediate MoS_2 layers causing a more lattice defect governed exfoliation of bulk MoS_2. Eventually the Au-MoS_2 bonds become weaker than those in the bulk MoS_2. This results in the exfoliation yield to drop to almost nothing [26]. Not only contamination of the gold surface causes the monolayer exfoliation yield to decrease rapidly, the surface roughness of the gold also weakens the Au-MoS_2 bond. This is due to the increased physical separation at surface depressions between the gold and the sulphur. It is therefore essential that the Root Mean Squared of the roughness of the gold is maximally of the order of 1 nm for an area of 500x500nm [26].

3.2 Sample fabrication

3.2.1 Gold

Two types of gold substrates were used; microplates and foil. Their single-crystalline nature and roughness below 1 nm [24] make gold microplates (see section A.1) ideal for imaging in LEEM. Due to their size (50 to 100 µm) it is however necessary to transport them onto a silicon(100) wafer (figure 3.3) for imaging purposes. This transportation is done using the stamping technique described in section 3.1.1.

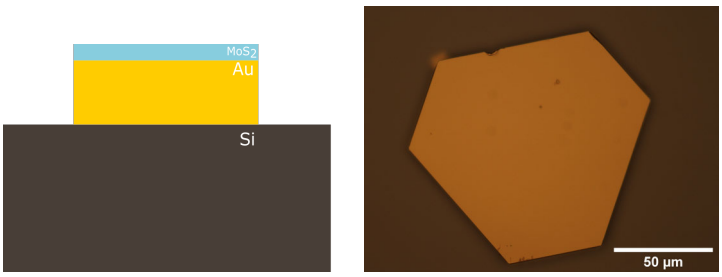

Figure 3.3: *(a) A schematic representation of the monolayer MoS_2 on top of Au microplatelet upon a Si(100) wafer. (b) Optical microscopy image of a gold microplate on a Si(100) wafer.*

Another option is to use gold foil (99.95% pure and 0.1 mm thick) which makes the use of a silicon wafer and a transfer process unnecessary. This results in a cleaner procedure. The gold foil however, is not in the (111)-orientation nor is it flat enough. In order to achieve the desired crystal structure and flatness the gold foil is rolled out. This rolling process adds energy to the system which allows the atoms to rearrange in their favoured (111)-crystal orientation. Even though the sample will not completely become single crystalline, the areas are typically large enough for LEEM measurements. Optically this change is visible as the gold starts shimmering. Using an optical microscope the effects of this rolling can be visualised on a smaller scale (see figure 3.4) which shows a smoothing of the overall surface.

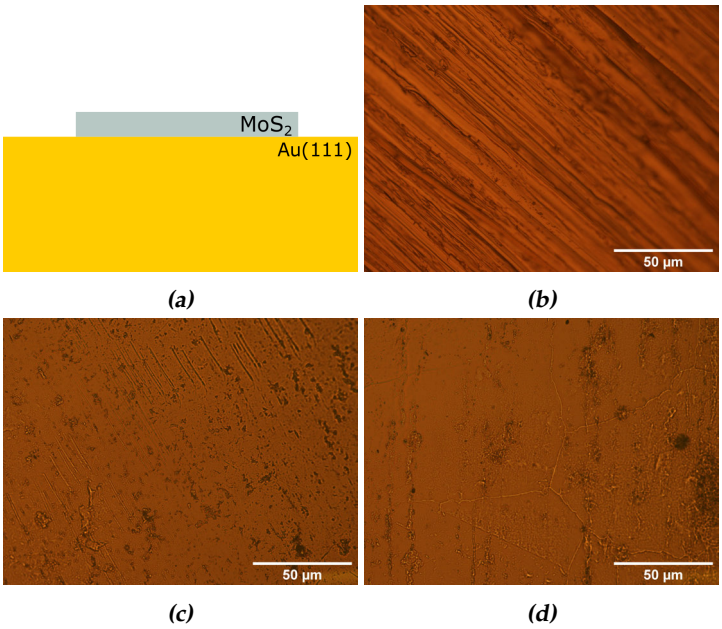

Figure 3.4: *(a) Schematic representation of the sample. (b-d) Optical microscopy images of the various states of the gold foil: (b) unprocessed, (c) rolled and (d) rolled and heated till approximately 530°C in ultra-high vacuum.*

The eventual phase transition relies on the bonds between the gold surface and monolayer MoS_2. It is therefore necessary to clean the gold surfaces as it is known that the adsorption of organic, airborne contaminants causes a clean gold surface to turn from hydrophilic to hydrophobic changing the surface reactivity [27]. As demonstrated by Raiber et al., cleaning gold with an hydrogen plasma regenerates a surface indistinguishable from a pure gold surface because it removes the sub-monolayer of hydrocarbon contamination [28]. However, surface contamination is a quick process. For bonding between gold and MoS_2 the exfoliation must be done within 10 minutes of cleaning the surface[26].

The plasma cleaning of gold is therefore an important step. In a plasma chamber, gas gets supplied with energy which causes the atomic shells of the gas to break down and charged particles to be created. This charged gas is called a plasma. The plasma can alter the surface through three different effects: ion-bombardment can remove the surface, ionized gas can chemically react with the surface and the UV radiation can break down carbon compounds. Which combination of effects is achieved during cleaning depends on the set plasma parameters such as pressure, selected gas and the plasma power. A method to protect the sample from getting bombarded by ions is by using a Faraday cage [29]. For this research it is important that only the contaminations are removed so therefore optimal plasma conditions must be found.

3.2.2 Molybdenum disulphide

The next step in the fabrication process is the deposition of monolayer MoS_2 on gold. These monolayers can be isolated in a multitude of processes; one can for example chemically grow the monolayers[30], exfoliate the monolayers from a bulk crystal using scotch tape[31] or exfoliate directly on the gold (section 3.1.2). As wet chemical processes are difficult and often result in lower quality monolayers, the exfoliation methods are used in this research.

The most reliable method is direct exfoliation from a bulk crystal. To extract a monolayer a piece of tape is brought in direct contact with the MoS_2 crystal cleaving some layers off. To isolate monolayers, the extracted bulk is cleaved multiple times using tape (for detailed information see appendix A.3.1). Inadequate exfoliation leads to thicker MoS_2 whilst excessive exfoliation leads to very small monolayers. It is therefore essential to find the right balance. In order to optically identify the monolayers, the exfoliated MoS_2 get transferred onto an oxidized silicon wafer. This is done by placing the tape on the wafer and heating it to 90°C before separation in order to minimize tape residues (figure 3.5). The identified monolayers, finally get transferred onto the gold using the stamping setup once more.

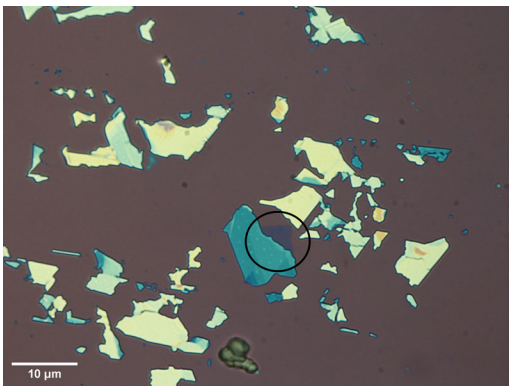

Figure 3.5: *Exfoliated MoS_2 on SiO_2. The circle indicates the monolayer.*

A cleaner but more unreliable method is to exfoliate the MoS_2 directly onto the gold surface. Through the preparation of a Nitto tape with bulk MoS_2 (see appendix A.3.2) the MoS_2 can be brought in contact with the gold immediately after the plasma cleaning using the gold-mediation exfoliation technique as described in section 3.1.2. The direct application after plasma cleaning largely prevents gold surface contamination.

3.2.3 Samples

Using the afore mentioned methods and materials the following six samples have been created. Samples 1 to 4 are cleaned using a capacitive coupled plasma chamber (FEMTO, Diener Electronic) with a hydrogen plasma at a pressure of 0.5 mbar for 5 min. Samples 1 and 2 consist of a microplate with stamped monolayers on top. Both are cleaned at a 100 W plasma but for sample 1 a Faraday cage is used whilst sample 2 is cleaned without. The essential difference between both samples is in the measurement techniques as sample 1 has been heated whilst measuring whereas sample 2 was annealed first. This was done to study the effect the electron beam has on interfacial dirt.
Samples 3 and 4 consist of a microplate where the MoS_2 has been exfoliated on directly. Both samples were cleaned with using a Faraday cage but sample 3 was cleaned at 20 W plasma whilst for sample 4 100 W was used.
Finally samples 5 and 6 consist of gold foil with directly exfoliated MoS_2 on top. Due to risks of plasma chamber contamination and hydrogen shortages a TVA Tepla 300 microwave plasma system with argon has been used. The system was set at a pressure of 0.02 bar, a flow of 200 $mLmin^{-1}$ and a power of 600 W. Sample 5 was cleaned using a Faraday cage whilst sample 6 was not.

Chapter 4

Measurement techniques

4.1 Atomic Force Microscopy

To get an indication of the gold RMS roughness, AFM measurements were made. An AFM is based on the interacting forces between the sample and a probe. The probe is a cantilever with a tip mounted on top. The tip has a height of the order of microns and a radius of the order of a few nano meters. When the probe is brought in close proximity to the sample, interaction forces between the tip and sample start to deflect the cantilever. This happens according to Hooke's law, which states that the deflection of the tip is linearly dependent on the applied force. The dominant force on longer ranges is the attractive van der Waals force which arises from electromagnetic field fluctuations between tip and sample. When, however, the tip and sample are very near the forces become repulsive due to Pauli and ionic repulsion [32]. The deflection of the cantilever is measured using a laser reflected from the backside of the cantilever as demonstrated in figure 4.1. The surface height can be calculated from this measured deflection [33]. To create a height profile of the sample, the tip is scanned over the sample in a line based pattern.

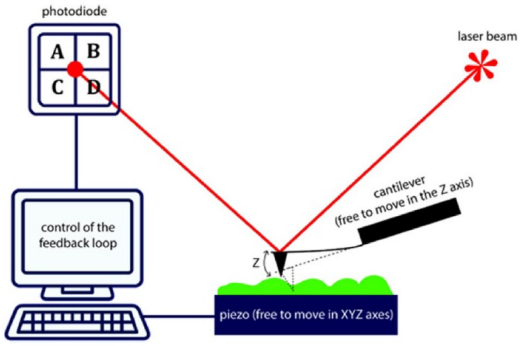

Figure 4.1: *A schematic figure of the AFM. The laser beam is pointed towards the back of the cantilever tip and reflected onto a photodiode. The interaction between the tip and sample causes the reflection to shift which in turn gives information on the height profile. The whole system is controlled using a feedback loop which in turn is dependent on the imaging mode.*
Taken from [33].

There are different modes for measuring. The first option is to measure in contact mode. In this method the repulsive force between tip and sample is measured and kept constant using a feedback signal. Subsequently, this feedback signal can be used to determine the height differences. A common problem that arises is the formation of a meniscus. This is due to capillary condensation which causes the tip to be attracted towards the surface. Therefore, a large force is generated on the sample: the contact between tip and sample causes compressive forces and the lateral scan movement induces shear forces. A major setback of this technique is therefore the risk of damaging both tip and sample [34]. As gold is known to be a soft metal and therefore susceptible to damage, a second technique was used.

A standard more gentle measurement technique is called ”tapping mode”. In this mode the cantilever is set to oscillate at (almost) its resonance frequency such that it taps the surface on each oscillation [34]. The oscillation amplitude changes when the distance between sample and tip varies due to the attractive van der Waals forces, giving a measure for height differences. The height profile is measured through a constant oscillation amplitude using a feedback loop [33]. From this profile, it is possible to extract the Root Mean Squared (RMS) roughness. The RMS roughness is a scale dependent measure for deviations from the height mean and is therefore a method for quantifying the smoothness of a surface.

No imaging technique, however, is without its fault. One of the more prominent artefacts is hysteresis or piezo creep in the imaging which results in compression or expansion of the features. Luckily, the used AFM setup contains a linearised sensor channel which largely reduces this artefact. Most other common artefacts are related to the size of the tip. When the radius of the tip is too

big or when the tip becomes blunt due to regular use, edges become smeared out because of the interaction between the (local) highest point of the sample and the sides of the tip (see figure 4.2(a)). Therefore, a smaller, pointier tip will reduce many of these artefacts. Contamination of the tip due to dirt on the sample, such as hydrocarbons, can also blunt the tip and introduce extra artefacts. This contamination can cause anomalously shaped structures to be present on the AFM signal as demonstrated in figure 4.2(c).

A final major artefact is the overshoot of edges in the sample (such as the edge of the gold in the samples used for this research). The overshoot makes steps in the surface more pronounced. Because the tip will recover itself and continue scanning at the correct height, often no information is lost figure 4.2(b)). This overshoot has two possible causes. When the effect is lessened by lowering the scan rate, it is an effect of piezoelectric scanner hysteresis and inertia of the cantilever holder. When slowing the scan rate does not decrease the effect, it is caused by additional attractive forces on the effective sample-tip force [35].

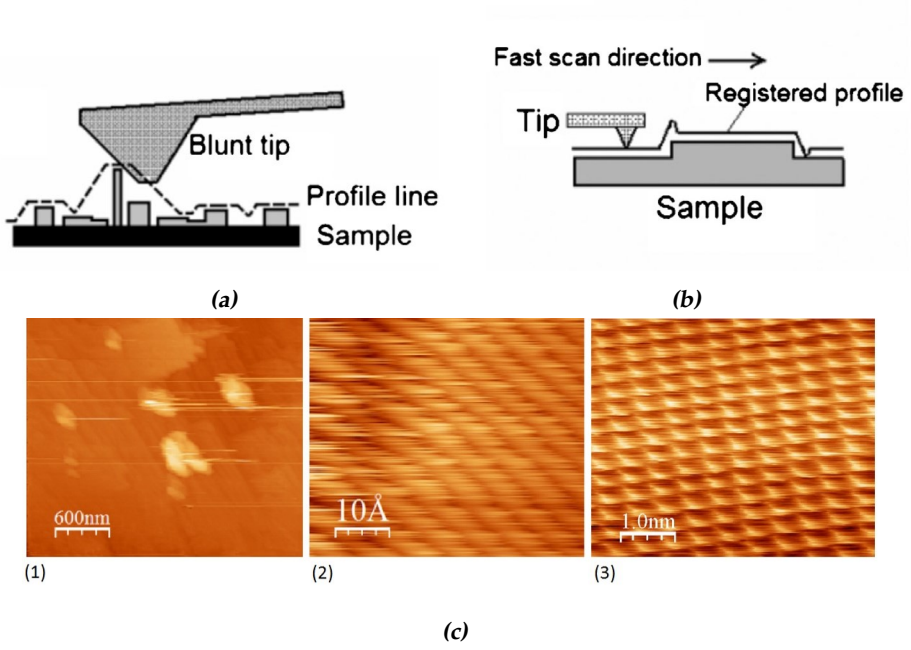

Figure 4.2: *Illustrations of common AFM artefacts. (a) The image artefact that broadens edges and possibly hides features due to a blunt tip (or a tip with an oversized large radius). (b) Overshoot of edges present in the sample. (c) An AFM image of a LiF crystal surface taken under ultra-high vacuum conditions. Image 1 and 2 illustrate noise induced by tip contamination. In image 3 the tip contamination is significantly reduced. All figures were adapted from [35].*

4.2 Low Energy Electron Microscopy

The most important imaging technique to acquire in situ images of the phase transition is Low-Energy Electron Microscopy (LEEM). LEEM is a direct imaging technique in which the image is formed using reflected electrons from a sample illuminated by an electron beam. Subsequently, the image is projected onto a detector using electromagnetic lenses. This results in detection of the whole beam, eliminating the need for any scanning method [36]. Low energy electrons are used as they impose much less damage to the samples and contain spectroscopic info. This makes LEEM an ideal technique for dynamic surface studies such as a phase transitions [37].

The electrons used to image are emitted from a cold field emission gun at 15 keV. The electron beam is deflect towards the sample using a square magnetic prism array (as illustrated in figure 4.3). In order to reflect from the sample surface, electrons are decelerated to low energies. This is achieved by applying a tunable negative voltage of -15 keV+V_0 between sample and objective lens. The so called cathode objective lens configuration [36] allows for a selected low electron energy range between 0 and 100 eV. After reflection, the electrons are accelerated again by the same difference of electric field and deflected 90° by the magnetic prism array. This way the beam continues towards the detector from the other end of the prism than the incoming beam. Multiple electromagnetic lenses are used at different locations in the beam path to assure that the electron beam is well-defined and collimated [38]. To furthermore keep the beam this well defined and to prevent unwanted interaction to occur the measurements were done at ultra-high vacuum ($p \approx 10^{-10}$ mbar). A feature of the LEEM set-up (ESCHER, Leiden Center for Ultramicroscopy) used for this research is the addition of an extra beam splitter and electron mirror. This is done to correct the aberration of the cathode objective lens; one of the major limitations in LEEM resolution. This results in resolutions up to 1.4 nm. It is furthermore possible in situ heat the samples up to temperatures of approximately 1800 K, making it possible to, for example, study phase transitions or growth processes.

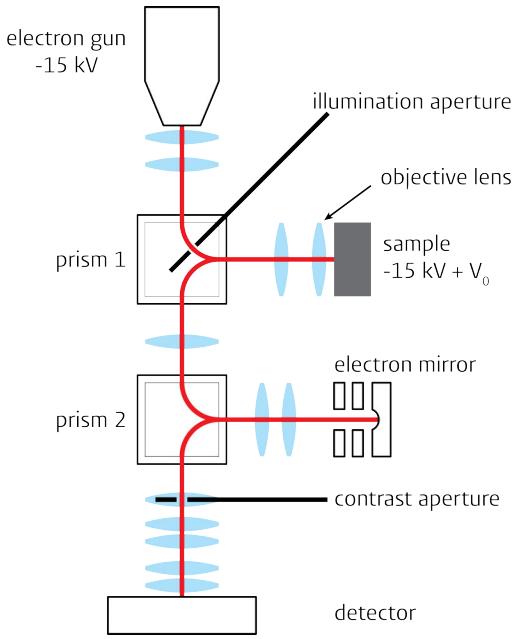

Figure 4.3: *A simplified scheme of the LEEM setup. The e-gun ejects electrons which travel via a set of lenses (in blue) along the red trajectory to the sample and detector.*

The LEEM setup has many different imaging modes which are easily interchangeable. Therefore, measurements consists of a combination of these modes. The most straightforward imaging technique is measuring the differences in reflection intensity over the sample (figure 4.4(a)).
Another option is to image in reciprocal space. This allows for analysis of the crystal structure of materials as the crystalline material diffracts the electron beam. The diffraction from a well defined atomic structure leads to constructive interference. When these electrons leaving under the same angle are focused, a low energy electron diffraction (LEED) pattern appears as demonstrated in figure 4.4(c). It is therefore possible to use this LEED pattern to identify 2H and 1T' MoS_2 and gold.
Some electrons, however, are inelastically scattered. These electrons have random energy and momentum but are still depicted. Therefore, they are visible as an uniform background disk. The radius of this disk increases for higher electron energies. This is due to the increasingly large amount of possible inelastic processes or decay pathways which result in a wider distribution of random energies and momenta. This background disk is called the Ewald sphere and it's radius is given by $|\mathbf{k}| = \frac{\sqrt{2m_e E_k}}{\hbar}$ (equation 2.1) [21].

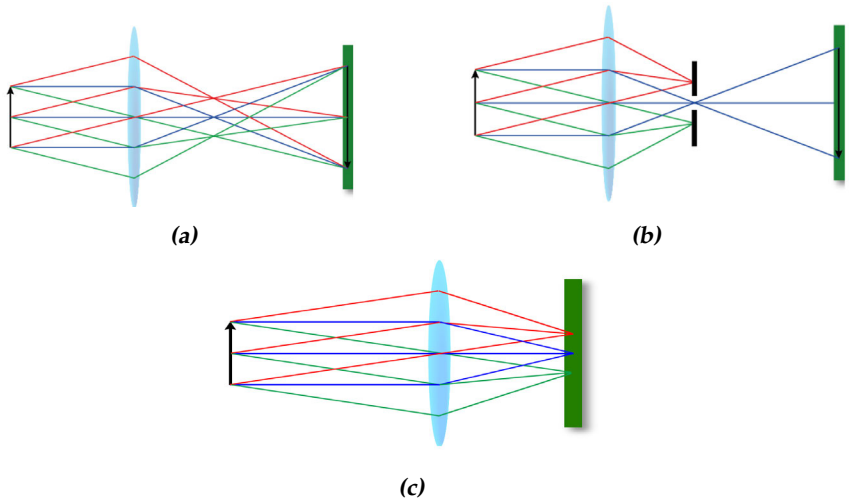

Figure 4.4: *Simplified ray diagrams representing the different imaging techniques. Figure (a) represents real space LEEM, (b) represents bright field LEEM and (c) represents diffraction LEEM (LEED).*
Adapted from [36]

The LEED pattern can be used to gain further insights in the measured material. The size of the unit cell and the crystal symmetries can be calculated from the pattern and energy in which the primary spots appear through the aforementioned calculation (section 2.2).
Measurements of the intensity of the LEED spots over different energies (the so called IV-curves) give a fingerprint for the measured material. These IV-curves are not only structure but also layer dependent [36]. The difference in electron spot intensity is determined by the scattering phase. However, it is difficult to calculate these intensities as the electrons do not scatter in a straightforward matter [39]. It is therefore necessary to do extensive computer simulations to create models. For 2H and 1T bulk MoS_2 some simulations have been done by Tim Iking and provide a reference for expected contrast differences between the different phases (figure 4.5) [40]. Furthermore, there are theoretical and experimental results on the IV-curves for different layer counts (figure 4.6). This makes it possible to further determine a layer count of the measured samples.

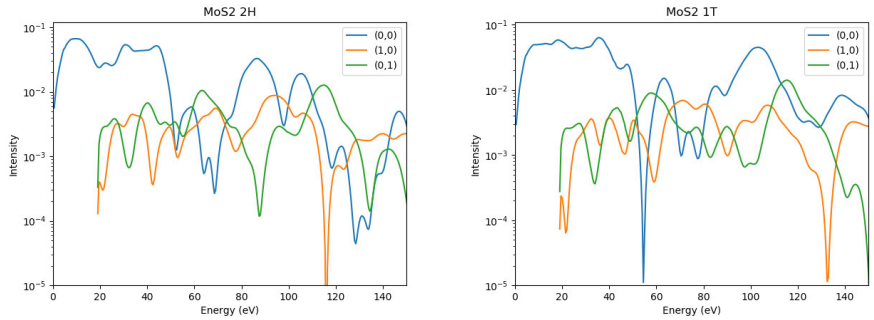

Figure 4.5: *Simulations of the IV-curves for primary and first order diffraction spots of bulk 2H (a) and 1T (b) MoS_2. The curves become increasingly reliable at higher energies [40].*

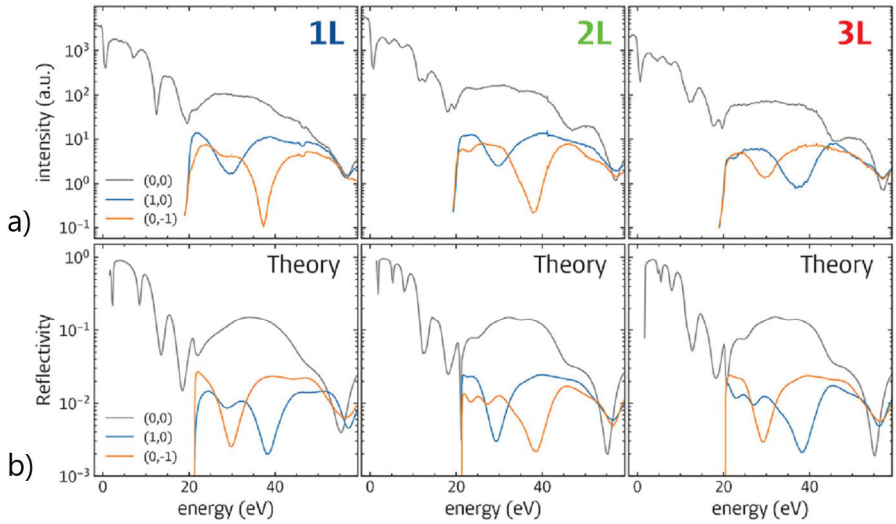

Figure 4.6: *Measured (a) and simulated (b) data of mono-, bi- and trilayer 2H-MoS_2. Adapted from [41]*

A major advantage of LEEM is the option to combine both reciprocal and real-space information. This can for example be done by selecting a small area in real space using an aperture (illumination aperture) and measuring the diffraction pattern. This is called microspot LEED (μLEED). Another option is to select only the central spot in LEED and to do LEEM imaging. This is called bright-field (BF) imaging and is depicted in figure 4.4(b). By selecting the central spot, only specular reflected electrons are imaged and contrast in the reflectivity amplitude and phase can be imaged. Different features become visible by adjusting the electron energy [36].

Another imaging technique is Photo Emission Electron Microscopy (PEEM). In this technique the sample is irradiated with ultraviolet (UV) light causing electrons to be ejected from the sample by the photoelectric effect. The image formed from these photoelectrons therefore indicates the variation in photoelectric effect over the sample. This variation is given by the work function of the materials; a higher work function yields a lower electron intensity. In terms of the MoS_2 on gold sample, it results in a larger overview image of the sample with enhanced contrast between gold and MoS_2 as compared to optical imaging.

Chapter 5

Results and discussion

5.1 Gold

As the roughness parameters of the gold are paramount, AFM and LEEM measurements have been performed on both microplates and foil before creating the desired samples including MoS_2.

5.1.1 Gold microplates

The intent of the AFM measurement was to characterize the height profile of the gold. As illustrated in figure 5.1 the gold has an edge height of approximately 0.4 µm. The height differences are investigated as the roughness parameters are important for both LEEM and gold-mediated exfoliation. When inspecting the measurements at different sized areas (figure 5.2) the typical RMS roughness is found to be below 1.5 nm. Notice the increasing roughness for smaller areas and the RMS roughness of 1.45nm for a 500x500nm area. Another feature (as visible in figure 5.3) is the dent at the middle of the microplate.

The intent of the LEEM measurements was to determine the crystallinity of the surface and to investigate the effects of heating. When looking at the measurements in bright field LEEM (figure 5.4), the lines and dots are the most striking features. The diffraction spots appear around 30 eV. When calculating the lattice constant with formula 2.6, a value of 4.5 Å is found. Furthermore, the diffraction appears in the expected hexagonal pattern for the (111) orientation. When looking at the rotation of the diffraction pattern it is noted that the shifts are only in the complete pattern (so there is also shift of the primary spot); there are no shifts of the primary spots with regard to the first order spots (figure 5.5). The IV at higher temperature seems more pronounced when looking at the energy dependent intensity curves at both 130°C and 512°C (figure 5.6).

Discussion

From the AFM data can be concluded that the increasing RMS roughness for smaller areas is probably due to surface contaminations. This is also visible in the dots in LEEM which are believed to be carbon contamination. The lines in the LEEM images, however, are the step edges in the gold, which indicate that the surface is reasonably clean. The carbon contamination reduces considerably after heating in ultra-high vacuum. This agrees with the more pronounced IV-curves at higher temperatures which are usually the result of a cleaner surface. The dots visible in AFM (figure 5.3(b)) are contamination from both air and the transfer process.
The gold is flat enough to properly measure in LEEM. The RMS roughness for a 500x500nm area is slightly above the 1 nm requirement for gold-mediated exfoliation. However, this method might still be applicable as plasma cleaning reduces contaminations and therefore lowers the RMS roughness. Furthermore, only a single monolayer with µm sizes has to be exfoliated instead of the cm sized flakes the Velický et al. aspire [26]. The measured dent, which is believed to be a nucleation point from the growth process, is large enough to avoid depositing monolayers MoS_2 on top, as it will make imaging in LEEM much harder.
As there is no clear difference between the IV-curves before and after heating (figure 5.6) it can be stated that the gold undergoes no structural changes. When the calculated lattice constant of 4.5 Å is compared to the theoretical value of 4.1 Å, it can be considered a reasonable value as it is within the expected error due to the distortion of the Ewald sphere at high energies. The diffraction pattern indicates that although the sample is not atomically flat (hence the moving primary spot), there is only one crystal orientation (hence no rotations in the diffraction pattern).
Therefore, it can be concluded that the gold is single crystalline in the (111) orientation and clean enough for exfoliation purposes especially after plasma cleaning and heating.

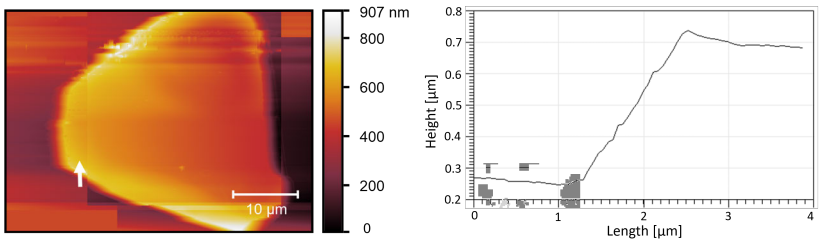

Figure 5.1: *(a) An AFM measured illustrative height profile of the gold microplate. (b) The height profile taken along the arrow in figure (a).*

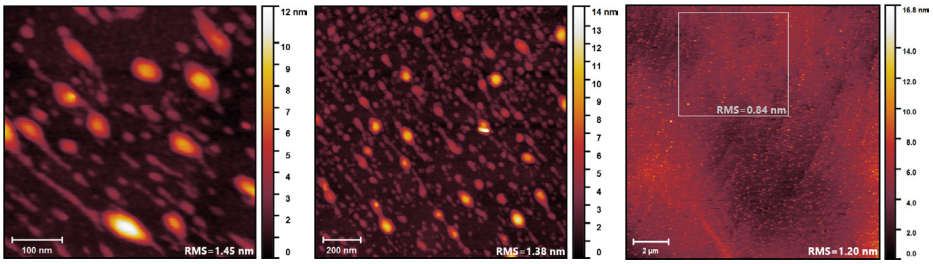

(a) **(b)** **(c)**

Figure 5.2: *AFM height maps of the gold particle surface after transfer onto the silicon. The grey inset (c) represents an area of approximately 6* µm *x 6* µm*, the order of the field of view in LEEM.*

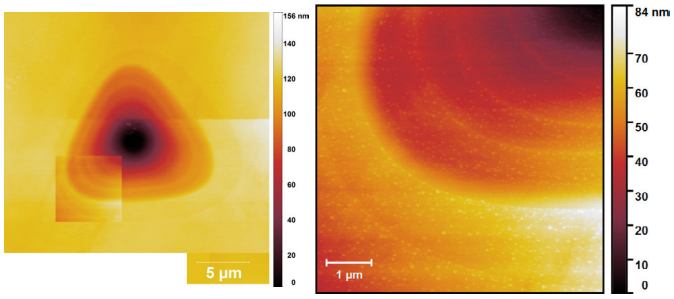

(a) **(b)**

Figure 5.3: *AFM image of the middle of a gold microplate before plasma cleaning. Figure (a) overview of the complete nucleation point, composed of 3 separate images. Figure (b) is the enlargement of the inset in image (a) and shows the steps in the dent.*

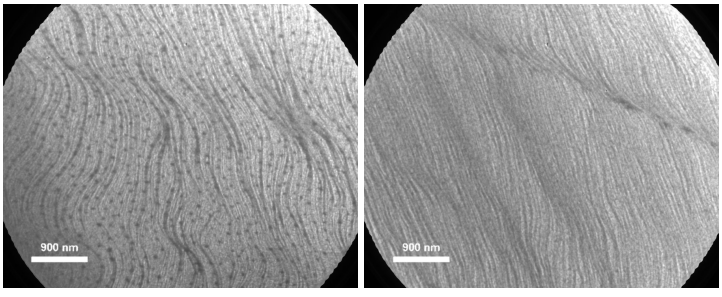

(a) **(b)** *T≈515°C*

Figure 5.4: *The surface of the gold microplate as observed in bright field LEEM imaging. Image (a) is taken at T≈130°C and E_k ≈2.3* eV *and (b) at T≈515°C and E_k ≈3.6* eV*. The lines are step edges in the gold and the black dots are believed to be carbon contamination.*

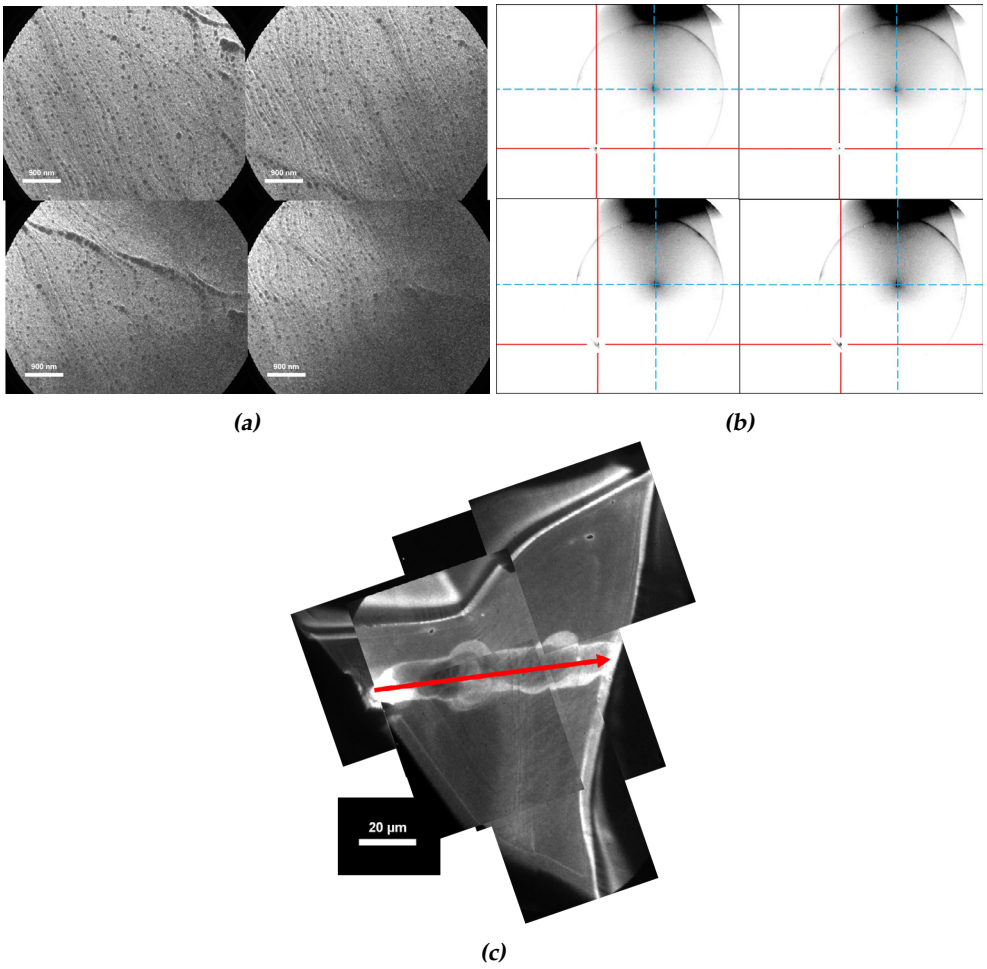

Figure 5.5: *Diffraction measurements at different places on the gold surface to indicate single-crystalline nature of the gold. Each LEEM image (a, $E_k \approx 4.97$ eV) belongs to the correspondingly placed LEED image (b). In the diffraction pattern visual guidelines of the primary (blue) and a first order (red) spot are placed to show the relative placement. The contrast of the first order spots is enhanced. The image of several stitched PEEM images (c) demonstrates the trajectory (along the red arrow) over the gold microplate in which the diffraction measurements are taken.*

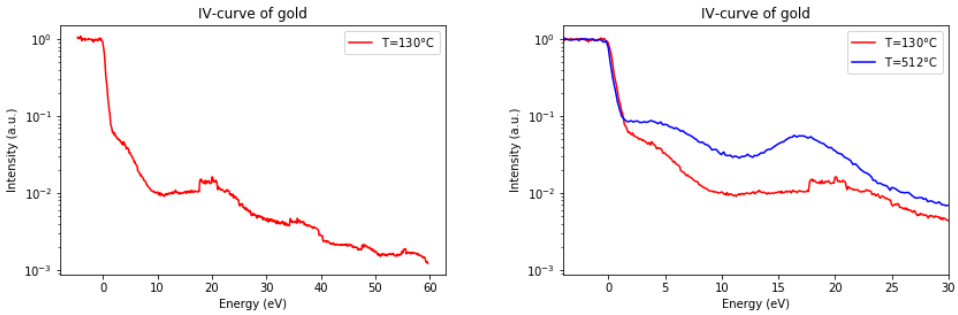

(a) *(b)*

Figure 5.6: *IV-Curves of the same gold surface as depicted in figure 5.5. (a) depicts the larger wider energy range whilst (b) compares the IV-curves at different temperatures on a smaller energy scale.*

5.1.2 Gold foil

When looking at different areas of rolled gold foil in AFM (figure 5.8), the differences in RMS roughness are striking. The RMS values differ between 0.88 nm and 4.28 nm for areas of 500x500 nm. The RMS roughness increases significantly when looking at a larger scales. Measurement in PEEM have been made of both the unprocessed and the rolled foil. When looking at the untreated foil (figure 5.7) no diffraction pattern is measured. PEEM measurements show the optically visible line pattern (figure 3.4) on the foils and the rough surface. After rolling, the line pattern is no longer visible. The LEED first order spots are only observed after rolling and tilting the beam (figure 5.9). The intensity of the first order spots is also lower when compared to the gold microplates.

Discussion

As for exfoliation purposes only few monolayers are needed and as micrometer-sized monolayers suffice, the unevenness of the sample is no problem as there are areas present that fulfil the RMS<1nm requirement. When, however, larger and more monolayers are required, this is an important factor to improve upon. The large RMS values for larger areas indicates that the sample is not flat on larger scales (opposed to the flat microplates).
The LEED measurements indicate that the rolling induces the (111)-orientation. The measurements of double diffraction patterns, however, indicates that the sample is not single crystalline which makes imaging more difficult. The single-crystalline areas are small (of the order of the electron beam) making both the gold-mediated exfoliation and imaging in LEEM difficult although not impossible. Figure 5.9 shows the primary and first order spots. The blue lines indicate the hexagonal lattice in the tilted figures. The various dark and light spots visible besides the indicated ones are image artefacts. The reduced intensity compared to the diffraction on microplates (where the first order spots were visible without tilting the beam) indicates that the crystalline orientation is less

defined than for the microplates.
It can be concluded that the quality of the gold foil for LEEM purposes is inferior to that of the gold foil albeit still workable.

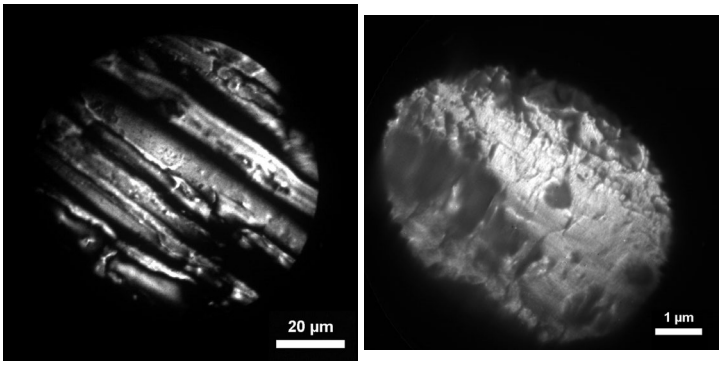

(a) ***(b)***

Figure 5.7: *PEEM (a) and LEEM ($E_k \approx 1.00$ eV) (b) images at different scales of the unprocessed gold foil.*

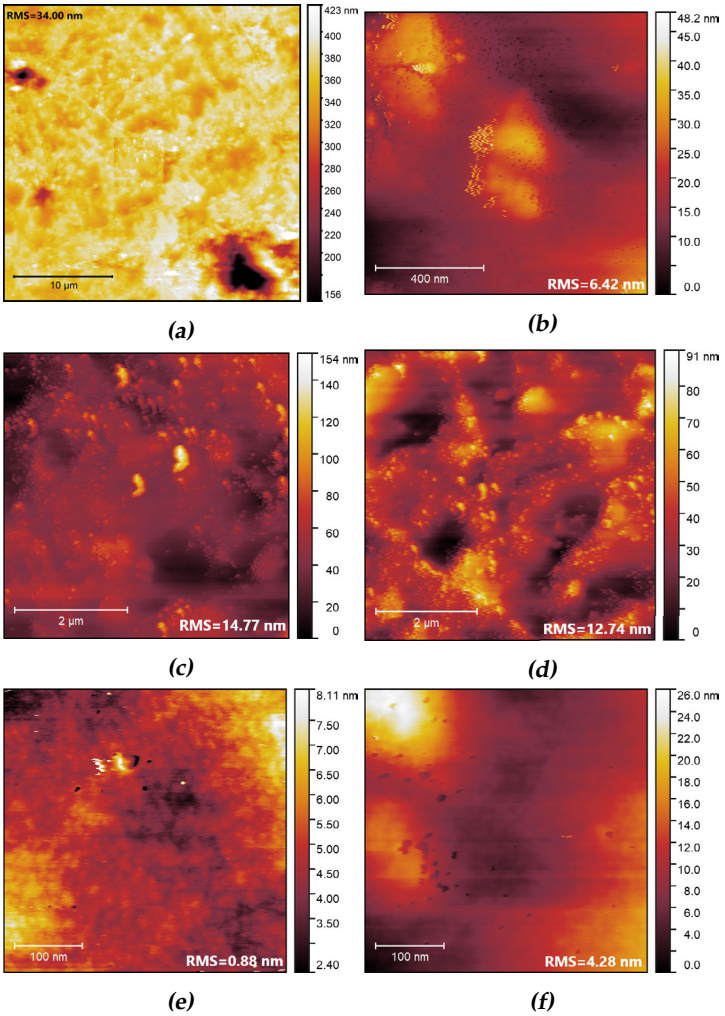

Figure 5.8: *AFM measurements of the gold foil. Indicative are the RMS roughnesses for the overall flatness and the differences in smoothness over the surface.*

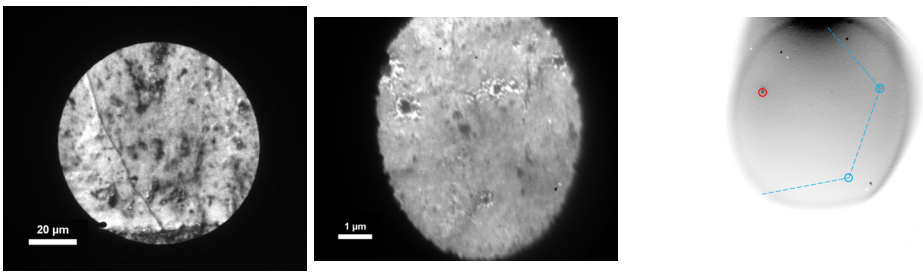

Figure 5.9: *PEEM (a) and LEEM (b, E_k ≈17.7 eV) images of the rolled gold foil. (c) Tilted diffraction pattern (E_k ≈32.8 eV) indicative of (111)-oriented gold. The primary spot is indicated in red and the first order spots in blue.*

5.2 Samples

The samples (section 3.2.3) are investigated using LEEM (and occasional AFM). The results are presented per sample type; first the stamped samples on gold microplates (sample 1 and 2), then the exfoliated samples on microplates (sample 3 and 4) and finally the exfoliated samples on gold foil (sample 5 and 6).

5.2.1 Stamped MoS_2 on gold microplates

First the completed samples have been inspected using an optical microscope to globally determine the success of the fabrication process (figure 5.10). For the stamped samples (1 and 2) the contrast between monolayers and gold is very small (see figure 5.10). After the stamping procedure LEEM measurements of the monolayers have been made. Diffraction (μLEED) measurements confirm the presence on 2H monolayer MoS_2 (figure 5.11). When compared to theory, the same IV-curve is measured although the intensities differ. The measurement furthermore shows that the first order diffraction spots become visible around 20 eV. When calculated using equation 2.7 a value of 3.1Å is found.
Whilst measuring, sample 1 was heated to 260 °C, approximately the ideal phase transition temperature [8]. Subsequently the sample was cooled down and reheated. However, all subsequent measurements show the same IV-curves (see figure 5.12). When looking at the sample in bright-field, a difference in structure between monolayer and bulk MoS_2 is observed. The sample is therefore also imaged in AFM (figure 5.13(c)) which shows a similar structure which is only present on the monolayer.

Sample 2 was heated before measuring (annealing) to prevent dirt getting trapped on the sample because of the electron beam. After each heating step a new area of monolayer MoS_2 was measured. The temperature was raised from 330°C to 390°C to 470°C and measurements were made after each heating step. No change in IV-curves was observed (figure 5.14). In sample 2, a slightly different IV-curve is measured which is identified as bilayer MoS_2. When looking at the IV-curve of gold, it is noticed that the features are suppressed as compared to the pure Au micro-platelets without transferred MoS_2.

Discussion

The measured lattice constant of 3.1 Å is a reasonable value when compared to the theoretical value of 3.16 Å which confirms (together with the IV-curves) the presence of 2H-MoS_2. The lack of change in IV-curves after heating (also when annealed before measuring) however demonstrates that no phase transition is observed.
The features on sample 1 can be concluded to be clusters of dirt on the surface. The differences in contamination structures between multi- and monolayer, however, may be caused by contamination at the interface between MoS_2 and gold as this type of contamination would be visible in monolayers but is obscured in the bulk. The AFM measurements confirm this suspicion by not only

measuring dirt clusters exclusively on the monolayer but also by displaying the same structures as measured in LEEM (see figure 5.13). These dirt clusters offer therefore also an explanation for the lack of phase transition as they prevent the Au-S bonds from forming.
The annealing step, which should allow the dirt to escape from the interface, is proven to be not strong enough as again no phase transition is measured. The increase in bright spots in mono- and bilayer as compared to sample 3 and lower heating temperatures however indicates that the annealing does remove some dirt. The suppression of the features in both gold and bulk MoS_2 further indicates that there is contamination present. The dirt could have been introduced by both insufficient plasma cleaning and by the stamping process.
Therefore it can be concluded that the stamped MoS_2 on gold microplates are too contaminated at the interface for the phase transition to occur and that only annealing is not sufficient enough to achieve the desired interfacial cleanliness.

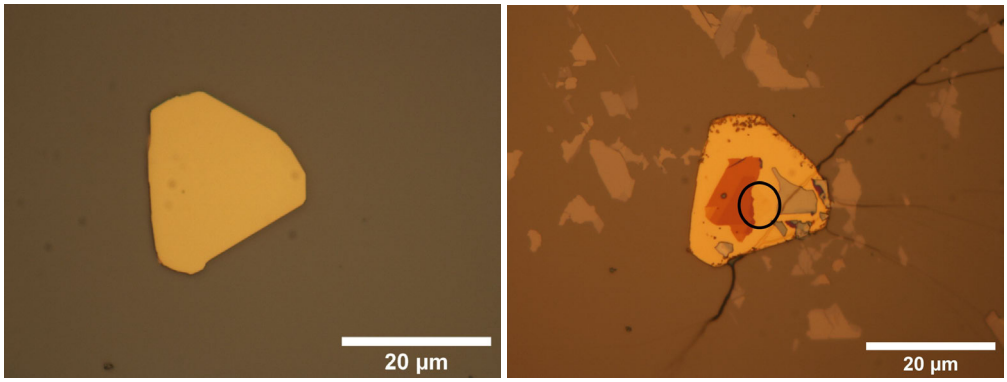

Figure 5.10: *Optical images of sample 1 before and after plasma cleaning and stamping. Image (a) depicts the situation before and (b) after. In (b) the same monolayer as depicted in 3.5 is stamped upon the gold and indicated by the black circle.*

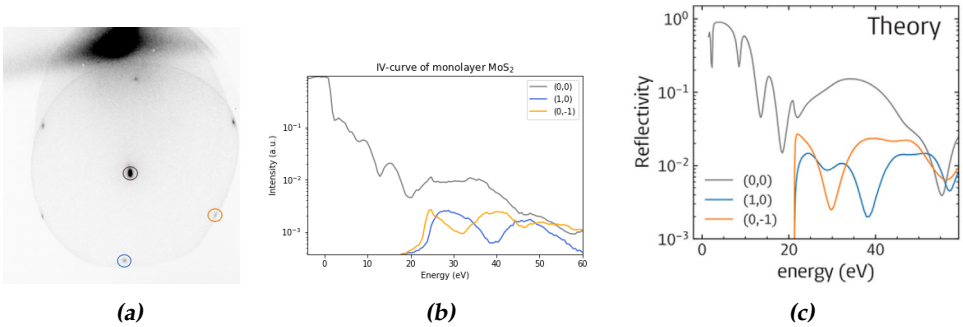

Figure 5.11: *Figure (a) depicts the visible diffraction pattern when measuring the monolayer. The coloured circles correspond to the measured IV-spectra for these spots in figure (b). The measured values can be compared to the theoretical curves (c) taken from [41].*

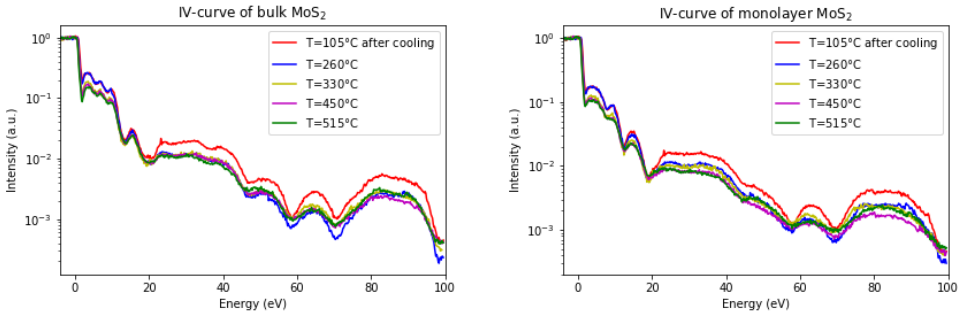

Figure 5.12: *IV curves of both monolayer and bulk MoS_2 measured at different temperatures. Figure 5.13(c) depicts the measured monolayer and bulk.*

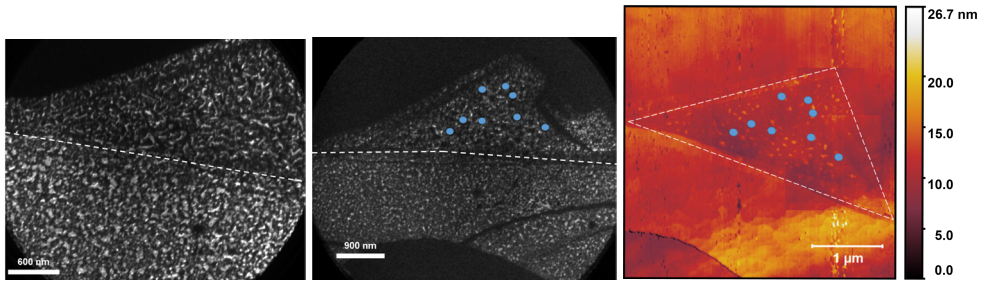

Figure 5.13: *(a,b) BF images of monolayer and bulk MoS_2 (b, $E_k \approx 4.0$ eV). The dashed lines indicate the border between monolayer and bulk with the monolayer situated above. (c) AFM image of the measured monolayer. The blue dots in (b,c) indicate the some of the identical structures in LEEM and AFM.*

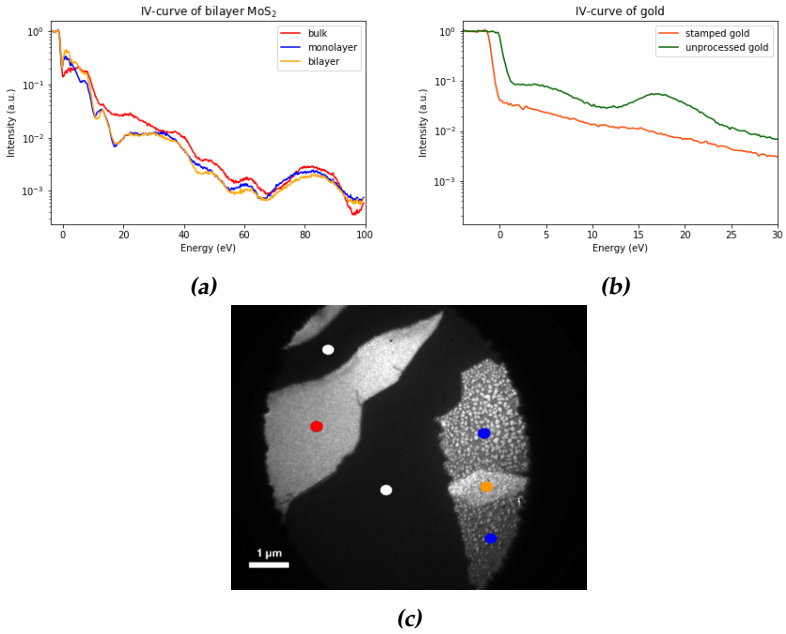

Figure 5.14: *IV curves of the different layers counts of 2H-MoS_2 after annealing at 470°C (a). The coloured dots on the BF image (c) correspond to the layer count in the IV curve. The white dots correspond to the gold. In figure (b) the measured gold curve is compared to the curve at 512 °C in figure 5.6*

5.2.2 Exfoliated MoS_2 on gold microplates

Optical microscopy of the samples with gold-mediated MoS_2 exfoliation shows distinct differences. Sample 4 (100 W) appears to have no MoS_2 whereas sample 3 (20 W) contains mainly bulk material (see figure 5.15). Remembering the contrast differences between monolayer and gold, it is still possible that there are (small) monolayers on sample 4. Further investigation in PEEM of sample 3 shows that many structures become visible that were invisible in the optical microscope (figure 5.16). Scanning in LEEM reveals some small thinner monolayer flakes besides the bulk pieces. When heating these monolayers, however, no change in IV-cure is observed. PEEM and LEEM investigation of sample 4 also reveals that there are some thin MoS_2 layers present although no monolayers are found (figure 5.17). In both sample 3 and 4 gold diffraction spots were measured.

Discussion

The material visible on sample 3 in PEEM are polymer residues from the exfoliation tape. The bulk material on sample 3 may indicate that the cleaning was insufficient, resulting in interfacial bonds similar to the internal MoS_2 bonds (see chapter 3.1.2). The cleaning at 100 W can be considered more effective as almost no bulk is exfoliated. However, there is are also no other monolayer MoS_2 exfoliated which could be a result of the small exfoliated area (the microplates) and the roughness of the plates. The area that is suitable for exfoliation is further restricted by the presence of the nucleation point which roughens the surface.

For the monolayers found in sample 3 no phase transition is observed. This can be caused by the same interfacial dirt mechanism as before which also corresponds to the exfoliation of large amount of bulk materials. The combination of plasma cleaning at a higher power and gold-mediated exfoliation (sample 4), however, does create a cleaner gold surface as shown by the more pronounced IV-curve for gold as compared to the stamped MoS_2 case and the measurement of a diffraction pattern.
It can be concluded that the gold microplates are not suitable for gold-mediated exfoliation as their area is too small and their surface possibly too rough. It can furthermore be concluded that the gold-mediated exfoliation is a cleaner process than the stamped MoS_2 but that the gold-sulphur interface for a 20W hydrogen plasma still not clean enough for the phase transition to occur.

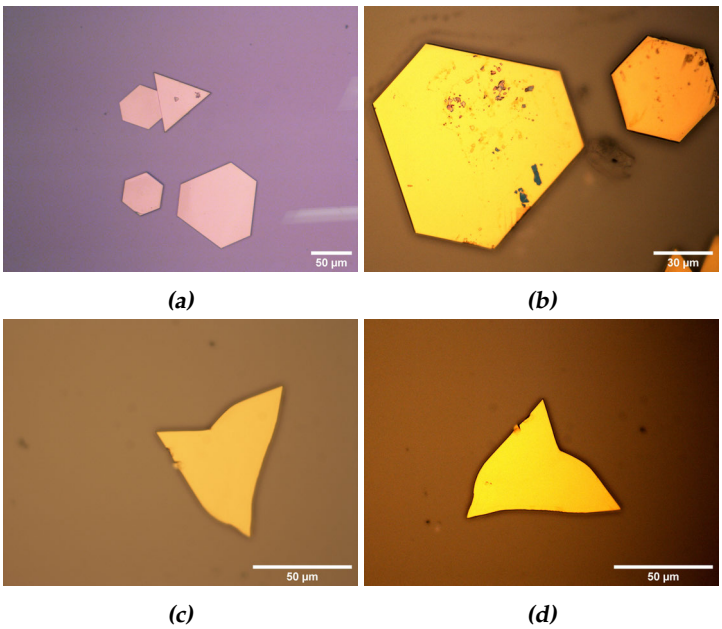

Figure 5.15: *Optical microscopy images of sample 3 (a,b) and 4 (c,d) before (a,c) and after (b,d) plasma cleaning and exfoliation.*

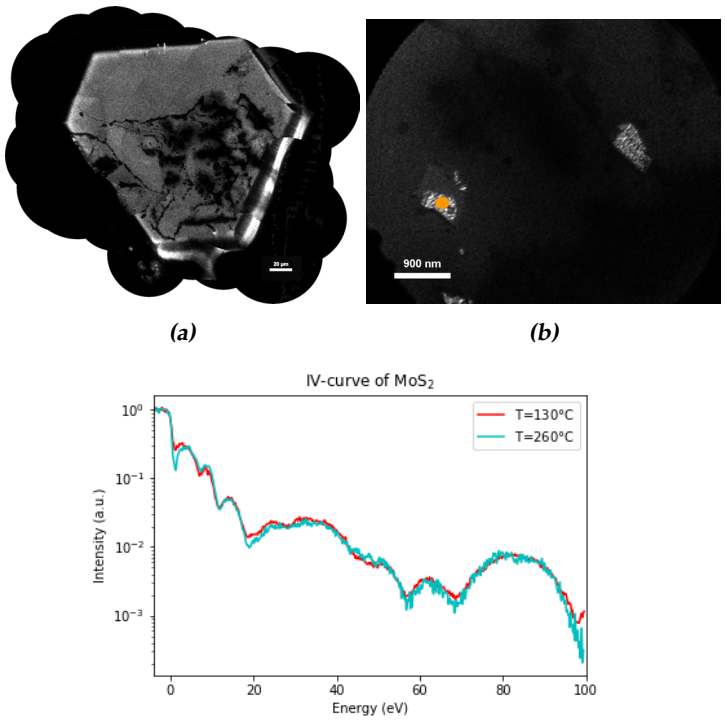

Figure 5.16: *(Stitched PEEM (a) and BF LEEM (b) images of the gold microplate cleaned at 20W before exfoliation. The LEEM images are an indication of the size of the thin layers present. Figure (c) shows the IV-curves of monolayer MoS_2 corresponding to the orange dot before and after heating.*

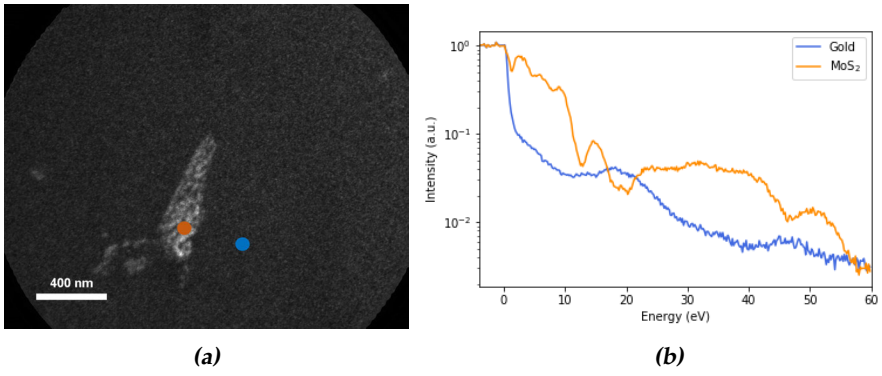

Figure 5.17: *(a) BF image of a small bulk flake on sample 4 with the corresponding IVs (b) of both flake and gold.*

5.2.3 Exfoliated MoS_2 on gold foil

Optical microscopy investigation of both gold foil samples (sample 5 and 6) reveals that some flake like forms are found but also that there are drastic changes to the gold surface for both samples as compared to the surface before plasma cleaning and exfoliation (figure 5.18). PEEM measurements of sample 6 show very rough surfaces (figure 5.19). In LEEM no diffraction pattern was found and no proper BF images could be taken.

Discussion

The change is structure of the gold surface could be explanation for the lack of exfoliated MoS_2. The switch to an argon plasma may be the cause for the structure change as argon has a much high atomic mass compared to hydrogen which results in a bigger impact on the gold. The change in plasma system (capacitive coupled plasma chamber to a microwave plasma system) further changes the impact of the plasma. The changes in the surface structure may however also have been caused by the differences in the (manual) rolling between both samples.
The lack of exfoliated MoS_2 can further be explained by the large variation in surface roughness of the gold foil. It must therefore be concluded that the low yield from the gold-mediated exfoliation technique on gold foil using an argon plasma is yet an unresolved problem.

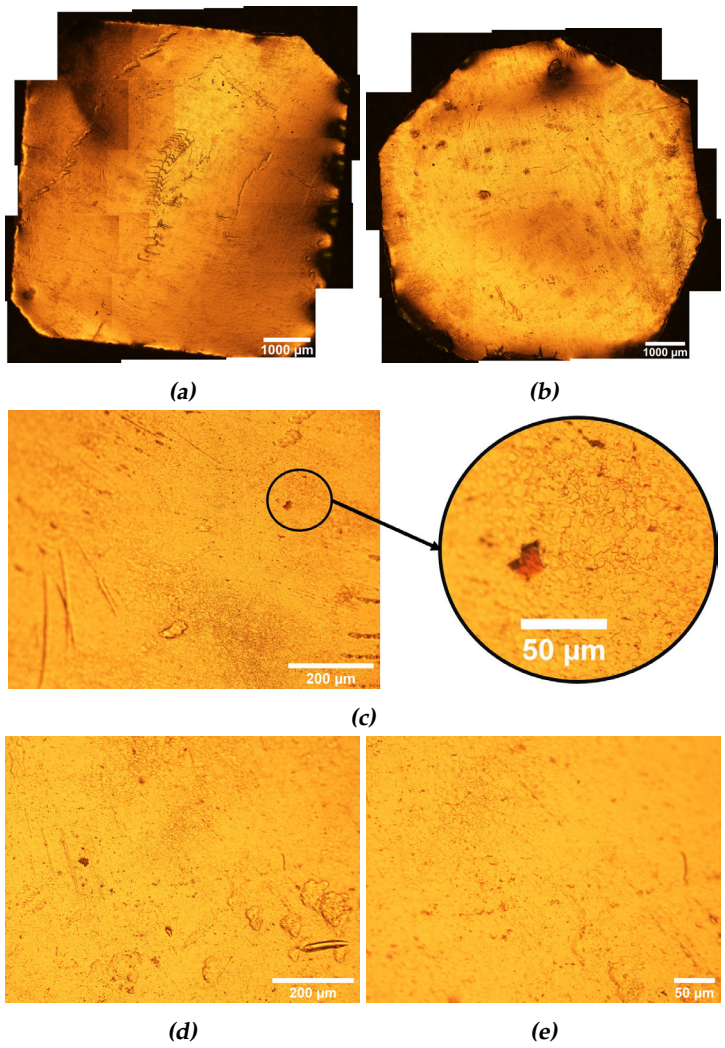

Figure 5.18: *(a,c) Optical images of sample 5 (b,d,e) and 6 (a,c)*

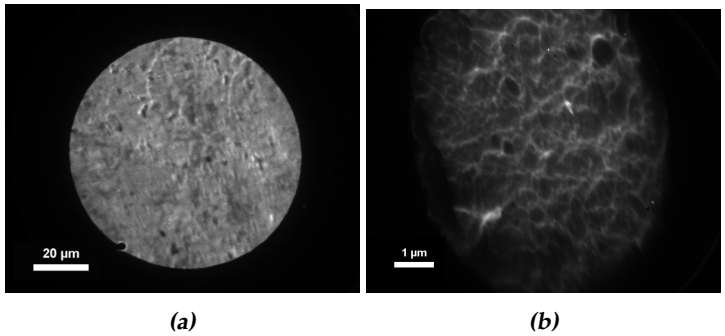

Figure 5.19: *PEEM (a) and LEEM (b, $E_k \approx 3.4$ eV) images of sample 6.*

Chapter 6

Conclusion and outlook

It can be concluded that the gold induced 2H to 1T′ phase transition of MoS_2 could not observed in any of the fabricated MoS_2 on gold samples. The absence of an observable phase transition might result from the difficulty in bringing gold and MoS_2 in close enough contact due to the roughness of the gold surface and contaminations at the interface. When comparing both gold foil and gold microplates, it can be concluded that microplates are better suited for LEEM imaging as they have a smoother surface (RMS$<$1.5nm). When comparing exfoliation techniques it can be concluded that the stamping on of tape-exfoliated MoS_2 monolayers is unsuccessful due to surface contaminations probably on both gold and MoS_2. The reason for the failed gold-mediated exfoliation is more unclear as both surface roughness of the gold and/or insufficient cleaning may be the cause.

In order to successfully measure the phase transition in the future, some changes must be made to the fabrication process. Improvements on the stamped monolayers could be achieved by creating a faster stamping procedure and by using a glove box to prevent dirt agglomeration. Both stamped and gold-mediated exfoliated monolayers could benefit from improved gold cleaning as cleaner gold stimulates Au-S bonding. It is therefore necessary to further explore the effects of (hydrogen) plasma on the gold surface. The greatest potential for improvement, however, is believed to be in the gold foils. A method must be found to further systematically flatten the gold foils until more areas with a RMS roughness$<$1nm are created. It is expected that exfoliation on these larger flat areas should lead to measurements of the 2H to 1T′ phase transition.

Acknowledgements

Sincere thanks go to many persons outside the research group who have helped during this research. The gold microplates are courtesy of Harald Gießen and Bettina Frank. Indispensable support on the hydrogen plasma is courtesy of the Schneider Research Group, especially Lin Jiang. Further gratitude for Thomas Schmidt and Julia Eckert for their help with de PDMS. I thank Federica Galli for support using the AFM. Finally I want to especially mention the whole Van der Molen Lab for the fruitful discussions and their support during this endeavour. A special acknowledgement should go to Johannes Jobst and Vera Janssen for their supervision and support throughout the project.

Appendix A

Experimental methods

A.1 Synthesis of gold microplates

The microplates were created by the group of Harald Gießen at the university of Stuttgart. The fabrication process is the following (see figure A.1): first the precursor tetraoctylammonium bromide in toluene (25 mmol/L, Au-ToABr) was coated onto doped silicon. Following thermolysis at 130°C the reduced Au is created. The sample is cleaned using toluene to remove the excess Au-ToAbr and thereafter in a H_2 plasma to remove any synthesis residues [24].

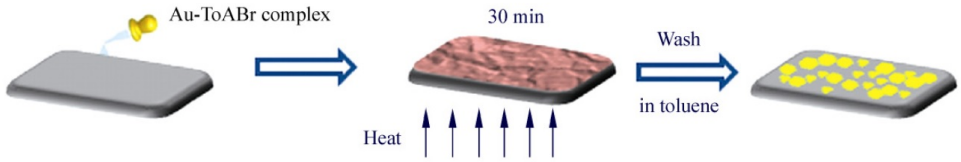

Figure A.1: *A schematic representation of growing process of the gold microplates [24].*

The gold microplates are delivered on doped silicon and consist of multiple gold particles with sizes ranging between 50 µm and 100 µm and thicknesses ranging between 30 nm and 1000 nm (see figure A.2) [24].

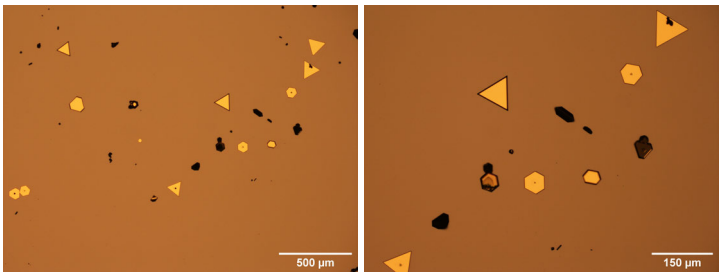

Figure A.2: *An optical image of the gold microplates on doped silicon.*

A.2 Stamping

The stamping procedure involves particles being picked up using PC dome on a glass slide. The glass slide is prepared in the following manner: (1) The glass slides are cleaned using acetone first, followed by isopropanol and dried using pressured N_2 to prevent residues from forming. (2) A form cut from PDMS is placed upon the clean slide. (3) The glass slide is heated for 1 minute at 90°C to further clean it. (4) A tape with PC is placed over the PDMS and the tape edges are firmly contacted to the glass slide. (5) The whole slide is baked again for a few minutes at at 90°C to ensure a reasonably clean surface. (6) The finished slide is placed upside down at the stamping set-up (see figure A.3) so it can be used.

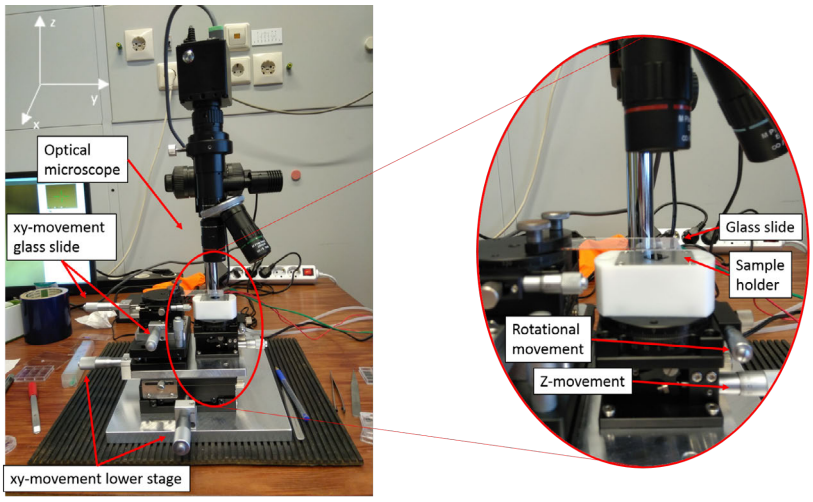

Figure A.3: *The stamping setup used for transferring gold particles. The glass slide is mounted above a stage which holds the sample using a vacuum. The glass slide can be moved and rotated in the xy plane. The stage with the sample can be moved in all directions, rotated in the xy plane and can also be heated. The optical microscope is mounted above the sample and glass slide and has magnifications of 5, 20 and 50.*

The PDMS triangles are created using a Gel Pak 4 box in which a two-dimensional triangle (for gold) or square (for MoS_2) is cut and lifted off using a razor blade(see figure A.4(a)). The triangle requires a 90° rotation before placement onto the glass slide such that on of the corners is pointing upwards (figure A.4(c)).
The PC tape is made from liquid PC. The liquid PC is spin coated upon SiO_2 at 4000 rounds per minute using the cleanroom facilities of LION. Before coating the SiO_2 wafers are sonicated first in acetone and then in isopropanol (both for 5 minutes) and blown dry using compressed nitrogen to ensure a clean surface. The solidified PC is prepared by cutting a small corner of the PC at the edge of the SiO_2 to create an adhesion point for the tape. Next a hole is made (using a hole puncher) in a piece of scotch tape. This hole is placed over the middle

of the spin-coated PC and the tape is gently pressed using a pair of tweezers. Following, the PC is pulled lose starting at the carved edge.
Before the transfer of the gold microplates on the silicon wafers, the wafers are cleaned in a similar way to the silicon oxide wafers. The only difference is in an extra cleansing step where the wafer is are submerged into chloroform for 1 minute before the compressed nitrogen cleaning.
The cleaning of the gold coated with PC on the silicon wafer is done using chloroform. The gold is cleaned by submerging the sample into the chloroform and letting it rest for approximately 1 minute. When the sample is taken out it is quickly blown dry using compressed N_2 to again prevent residues from forming.

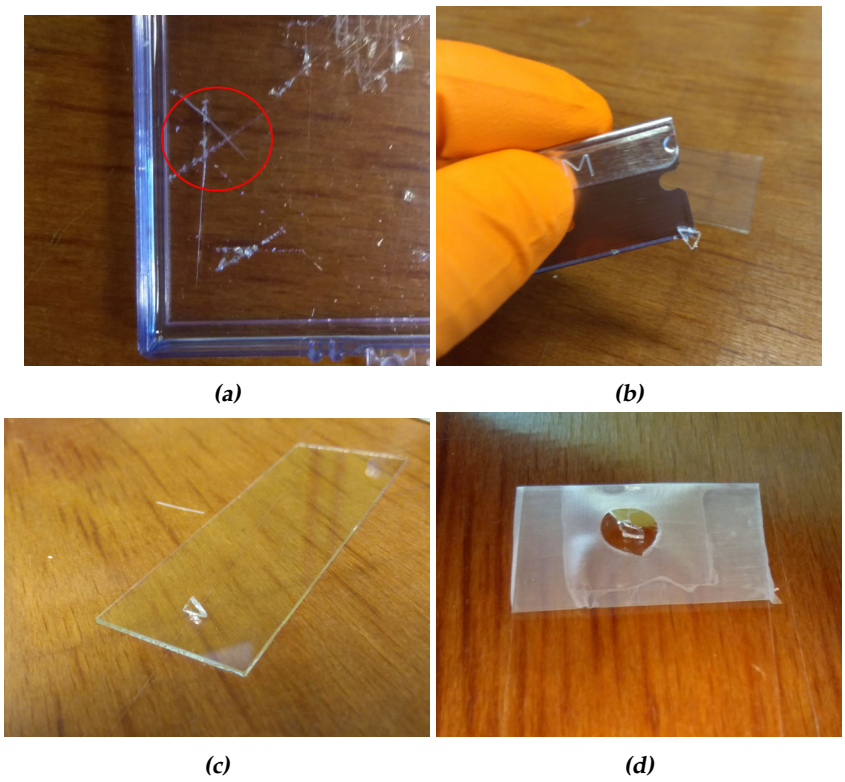

Figure A.4: *An optical representation of the moving of the PDMS triangles.*
(a) The two-dimensional triangle as cut in the Gel Pak 4 box indicated by the red circle.
(b)Transfer of the triangle to the glass slide using a clean razor blade.
(c) The rotated triangle on the clean slide.
(d) The finished glass slide with PC coated over the PDMS.

A.3 Exfoliation

A.3.1 Monolayer MoS_2

The monolayer exfoliation requires some MoS_2 to be transferred from the crystal using Scotch tape. The bulk MoS_2 is exfoliated on the Scotch tape 3 or 4

times after which it gets transferred onto Nitto tape and subsequently onto an oxidized silicon wafer with a 285 nm oxide thickness. During this exfoliation it is important that the tape is separated quickly whilst trying to minimize the strain on the tape. The extra exfoliation step from Scotch tape to Nitto-tape is due to the fact that Scotch tape is easier to exfoliate with whilst the Nitto-tape leaves less residues on the wafer. The tape is transferred on the silicon wafer and heated till 90°C to minimize the tape residues. Before depositing MoS_2 on the SiO_2 the wafer is cleaned the same way as the oxidized silicon wafers used for the PC coating (see section A.2).

Using an optical microscope monolayer MoS_2 is detected. This can be done by looking optically for transparent like layers and by subsequently looking at the contrast value differences from the brightness profile (figure A.5). For a monolayer MoS_2 on 300 nm thick oxidized silicon a normalized contrast drop of 8.9 (and a standard deviation of 0.2) is expected [42]. As 285 nm oxidized silicon is used a somewhat similar value is expected. When looking at the contrast difference of two monolayers with different white balancing conditions using the exact same processing technqiue as provided by Xiong et al. [42] an average contrast drop of 7 (standard deviation 2) is measured.

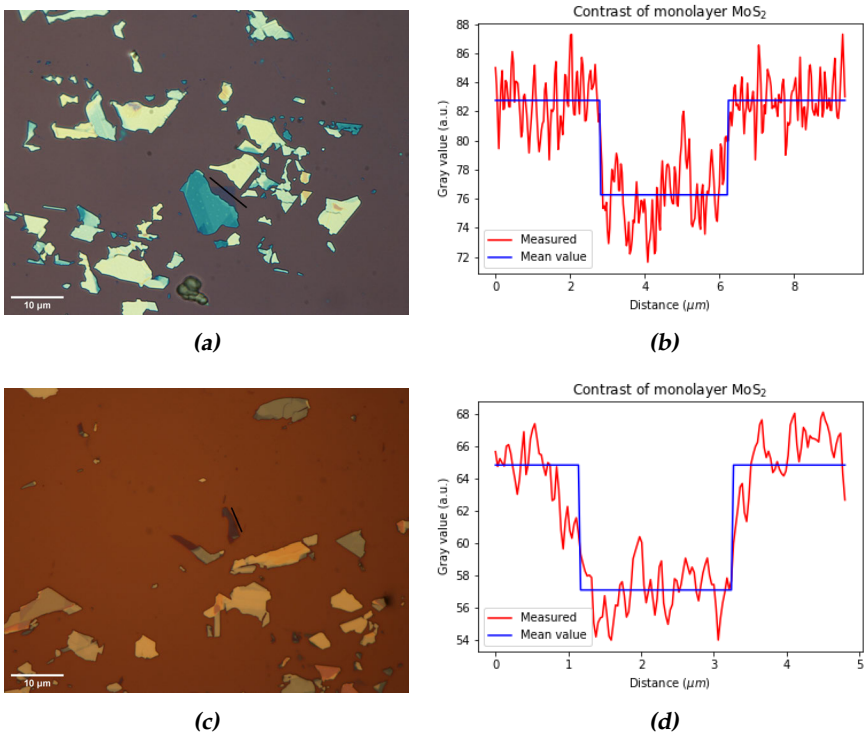

Figure A.5: *Contrast profiles of the monolayer MoS_2 on SiO_2. Both line profiles correspond to the lines drawn in the optical images. The mean curve fitted are the means of the monolayer and SiO_2 calculated separately.*

A.3.2 Gold-mediated exfoliation

For the gold-mediated exfoliation, some bulk MoS_2 is transferred from the crystal using Scotch tape. The bulk is exfoliated from the Scotch tape immediately onto Nitto-tape. During this exfoliation it is important that the MoS_2 stays as thick as possible (optically visible as a silver shimmering (figure A.6)). The extra exfoliation step from Scotch tape to Nitto-tape is owing to the fact that Scotch tape exfoliates more and thicker MoS_2 from the crystal whilst the Nitto-tape leaves less residues on the gold sample.
The Nitto-tape with bulk MoS_2 is placed upon the gold and softly pressed using a cotton tip immediately after the particle is taken from the plasma. Finally the sample with the gold is carefully but rapidly extracted from the tape, creating the desired sample for the LEEM measurements.

Figure A.6: *The Nitto tape with bulk MoS_2 as used for exfoliation*

A.4 Measurements

Sample 1 to 4 are cleaned using the capacitive coupled plasma chamber (FEMTO, Diener Electronic) of the Schneider Research Group at the Leiden Institute of Chemistry. Sample 5 and 6 have been created using an Argon plasma (TVA Tepla 300 microwave plasma system) at the Kavli Nanolab at the Technical University Delft.
The AFM measurements were performed in the AFM Facility of the Leiden Institute of Physics (LION) using the JPK Nanowizard 3 Ultra Speed AFM/STM. The images were acquired using a 70 kHz and 2 Nm^{-1} cantilever in tapping mode (AC). The images were processed using both JPK Data Processing software and Gwyddion 2.53.
The LEEM measurements were done at the ESCHER (Electronic, Structural and CHEmical nano-imaging in Real time) setup at the Leiden Center for Ultramicroscopy at Leiden University.

Bibliography

[1] K. S. Novoselov, A. K. Geim, S. V. Morozov, D. Jiang, Y. Zhang, S. V. Dubonos, I. V. Grigorieva, and A. A. Firsov, *Electric Field Effect in Atomically Thin Carbon Films*, Science **306**, 666 (2004).

[2] A. K. Geim and I. V. Grigorieva, *Van der Waals heterostructures*, Nature **499**, 419 (2013).

[3] P. Ajayan, P. Kim, and K. Banerjee, *Two-dimensional van der Waals materials*, Physics Today **69**, 38 (2016).

[4] X. Li and H. Zhu, *Two-dimensional MoS2: Properties, preparation, and applications*, Journal of Materiomics **1**, 33 (2015).

[5] W. Choi, N. Choudhary, G. H. Han, J. Park, D. Akinwande, and Y. H. Lee, *Recent development of two-dimensional transition metal dichalcogenides and their applications*, Materials Today **20**, 116 (2017).

[6] M. Chhowalla, H. S. Shin, G. Eda, L.-J. Li, K. P. Loh, and H. Zhang, *The chemistry of two-dimensional layered transition metal dichalcogenide nanosheets*, Nature Chemistry **5**, 263 (2013).

[7] W. Zhao, J. Pan, Y. Fang, X. Che, D. Wang, K. Bu, and F. Huang, *Metastable MoS2 : Crystal Structure, Electronic Band Structure, Synthetic Approach and Intriguing Physical Properties*, Chemistry - A European Journal **24**, 15942 (2018).

[8] X. Yin, Q. Wang, L. Cao, C. S. Tang, X. Luo, Y. Zheng, L. M. Wong, S. J. Wang, S. Y. Quek, W. Zhang, A. Rusydi, and A. T. S. Wee, *Tunable inverted gap in monolayer quasi-metallic MoS2 induced by strong charge-lattice coupling*, Nature Communications **8**, 486 (2017).

[9] D. Voiry, A. Mohite, and M. Chhowalla, *Phase engineering of transition metal dichalcogenides*, Chemical Society Reviews **44**, 2702 (2015).

[10] V. Giacometti, B. Radisavljevic, A. Radenovic, J. Brivio, and A. Kis, *Single-layer MoS2 transistors*, Nature Nanotechnology **6**, 147 (2011).

[11] S. Wi, H. Kim, M. Chen, H. Nam, L. J. Guo, E. Meyhofer, and X. Liang, *Enhancement of photovoltaic response in multilayer MoS2 induced by plasma doping*, ACS Nano **8**, 5270 (2014).

[12] J.-M. Yun, Y.-J. Go, J. Kim, Y.-J. Noh, H.-G. Jeong, T.-W. Kim, J.-S. Yeo, S.-S. Kim, S.-I. Na, S. Lee, H. Y. Koo, and D.-Y. Kim, *Efficient work-function engineering of solution-processed MoS2 thin-films for novel hole and electron transport layers leading to high-performance polymer solar cells*, Journal of Materials Chemistry C **1**, 3777 (2013).

[13] R. Kappera, D. Voiry, S. E. Yalcin, B. Branch, G. Gupta, A. D. Mohite, and M. Chhowalla, *Phase-engineered low-resistance contacts for ultrathin MoS2 transistors*, Nature Materials **13**, 1128 (2014).

[14] J. Jung, H. Bark, D. Byun, C. Lee, and D.-H. Cho, *Mechanical characterization of phase-changed single-layer MoS2 sheets*, 2D Materials **6**, 025024 (2019).

[15] I. Song, C. Park, and H. C. Choi, *Synthesis and properties of molybdenum disulphide: From bulk to atomic layers*, RSC Advances **5**, 7495 (2015).

[16] H. L. Zhuang, M. D. Johannes, A. K. Singh, and R. G. Hennig, *Doping-controlled phase transitions in single-layer MoS2*, Physical Review B **96**, 1 (2017).

[17] R. Kappera, D. Voiry, S. E. Yalcin, W. Jen, M. Acerce, S. Torrel, B. Branch, S. Lei, W. Chen, S. Najmaei, J. Lou, P. M. Ajayan, G. Gupta, A. D. Mohite, and M. Chhowalla, *Metallic 1T phase source/drain electrodes for field effect transistors from chemical vapor deposited MoS2*, APL Materials **2**, 092516 (2014).

[18] D. Voiry, M. Salehi, R. Silva, T. Fujita, M. Chen, T. Asefa, V. B. Shenoy, G. Eda, and M. Chhowalla, *Conducting MoS2 nanosheets as catalysts for hydrogen evolution reaction*, Nano Letters **13**, 6222 (2013).

[19] Y. L. Huang, Y. Chen, W. Zhang, S. Y. Quek, C. H. Chen, L. J. Li, W. T. Hsu, W. H. Chang, Y. J. Zheng, W. Chen, and A. T. Wee, *Bandgap tunability at single-layer molybdenum disulphide grain boundaries*, Nature Communications **6**, 1 (2015).

[20] X. Yin, C. S. Tang, D. Wu, W. Kong, C. Li, Q. Wang, L. Cao, M. Yang, Y.-H. Chang, D. Qi, F. Ouyang, S. J. Pennycook, Y. P. Feng, M. B. H. Breese, S. J. Wang, W. Zhang, A. Rusydi, and A. T. S. Wee, *Unraveling High-Yield Phase-Transition Dynamics in Transition Metal Dichalcogenides on Metallic Substrates*, Advanced Science **1802093**, 1802093 (2019).

[21] T. A. de Jong, *Stacking domains in bilayer Van der Waals materials*, Master thesis, Leiden University, 2017.

[22] P. J. Zomer, M. H. D. Guimarães, J. C. Brant, N. Tombros, and B. J. van Wees, *Fast pick up technique for high quality heterostructures of bilayer graphene and hexagonal boron nitride*, Applied Physics Letters **105**, 013101 (2014).

[23] B. S. Jessen, L. Gammelgaard, M. R. Thomsen, D. M. A. Mackenzie, J. D. Thomsen, J. M. Caridad, E. Duegaard, K. Watanabe, T. Taniguchi, T. J. Booth, T. G. Pedersen, A.-P. Jauho, and P. Bøggild, *Lithographic band structure engineering of graphene*, Nature Nanotechnology (2019).

[24] B. Radha, M. Arif, R. Datta, T. K. Kundu, and G. U. Kulkarni, *Movable Au microplates as fluorescence enhancing substrates for live cells*, Nano Research **3**, 738 (2010).

[25] S. B. Desai, S. R. Madhvapathy, M. Amani, D. Kiriya, M. Hettick, M. Tosun, Y. Zhou, M. Dubey, J. W. Ager, D. Chrzan, and A. Javey, *Gold-Mediated Exfoliation of Ultralarge Optoelectronically-Perfect Monolayers*, Advanced Materials **28**, 4053 (2016).

[26] M. Velický, G. E. Donnelly, W. R. Hendren, S. McFarland, D. Scullion, W. J. Debenedetti, G. C. Correa, Y. Han, A. J. Wain, M. A. Hines, D. A. Muller, K. S. Novoselov, H. D. Abruna, R. M. Bowman, E. J. Santos, and F. Huang, *Mechanism of Gold-Assisted Exfoliation of Centimeter-Sized Transition-Metal Dichalcogenide Monolayers*, ACS Nano (2018).

[27] T. Smith, *The hydrophilic nature of a clean gold surface*, Journal of Colloid And Interface Science **75**, 51 (1980).

[28] K. Raiber, A. Terfort, C. Benndorf, N. Krings, and H. H. Strehblow, *Removal of self-assembled monolayers of alkanethiolates on gold by plasma cleaning*, Surface Science **595**, 56 (2005).

[29] Diener Electronic, *Introduction to Plasma*, Retrieved from https://www.plasma.com/en/plasmatechnik/introduction-to-plasma/ **18-06-2019**.

[30] Y. H. Lee, X. Q. Zhang, W. Zhang, M. T. Chang, C. T. Lin, K. D. Chang, Y. C. Yu, J. T. W. Wang, C. S. Chang, L. J. Li, and T. W. Lin, *Synthesis of large-area MoS2 atomic layers with chemical vapor deposition*, Advanced Materials **24**, 2320 (2012).

[31] H. Li, J. Wu, Z. Yin, and H. Zhang, *Preparation and applications of mechanically exfoliated single-layer and multilayer MoS2 and WSe2 nanosheets*, Accounts of Chemical Research **47**, 1067 (2014).

[32] R. García and R. Pérez, *Dynamic atomic force microscopy methods*, Surface Science Reports **47**, 197 (2002).

[33] J. L. Toca-Herrera, *Atomic force microscopy meets biophysics, bioengineering, chemistry and materials science*, ChemSusChem **12**, 603 (2018).

[34] Q. Zhong, D. Inniss, K. Kjoller, and V. B. Elings, *Fractured polymer/silica fiber surface studied by tapping mode atomic force microscopy*, Surface Science **290**, 688 (1993).

[35] F. Gołek, P. Mazur, Z. Ryszka, and S. Zuber, *AFM image artifacts*, Applied Surface Science **304**, 11 (2014).

[36] J. Kautz, *Low-Energy Electron Microscopy on Two-Dimensional Systems: Growth , Potentiometry and band structure mapping*, Doctoral thesis, Leiden University, 2015.

[37] R. M. Tromp, *Low-Energy Electron Microscopy*, MRS Bulletin **19**, 44 (1994).

[38] R. Tromp, J. Hannon, A. Ellis, W. Wan, A. Berghaus, and O. Schaff, *A new aberration-corrected, energy-filtered LEEM/PEEM instrument. I. Principles and design*, Ultramicroscopy **110**, 852 (2010).

[39] K. Heinz, *LEED and DLEED as modern tools for quantitative surface structure determination*, Reports on Progress in Physics **58**, 637 (1995).

[40] T. Iking, *Identifying TaS2 polytypes with LEED simulation*, Bachelor thesis, Leiden University, 2019.

[41] T. A. de Jong, J. Jobst, H. Yoo, E. E. Krasovskii, P. Kim, and S. J. van der Molen, *Measuring the Local Twist Angle and Layer Arrangement in Van der Waals Heterostructures*, Physica Status Solidi (B) Basic Research **1800191**, 1 (2018).

[42] Q. Xiong, H. Li, G. Lu, X. Huang, X. Lu, J. Yang, H. Zhang, and J. Wu, *Rapid and Reliable Thickness Identification of Two-Dimensional Nanosheets Using Optical Microscopy*, ACS Nano **7**, 10344 (2013).